

Dense gas in nearby galaxies^{*}

XIII. CO submillimeter line emission from the starburst galaxy M 82

R.Q. Mao^{1,2,3}, C. Henkel¹, A. Schulz^{4,5}, M. Zielinsky⁶, R. Mauersberger^{7,8,9}, H. Störzer⁶, T.L. Wilson^{1,7}, and P. Gensheimer⁷

¹ Max-Planck-Institut für Radioastronomie, Auf dem Hügel 69, 53121 Bonn, Germany

² Purple Mountain Observatory, Chinese Academy of Sciences, 210008 Nanjing, P.R. China

³ National Astronomical Observatories, Chinese Academy of Sciences, Beijing 100018, P.R. China

⁴ Institut für Physik und Didaktik, Universität zu Köln, Gronewaldstrasse 22, 50931 Köln, Germany

⁵ Institut für Astrophysik und Extraterrestrische Forschung der Universität Bonn, Auf dem Hügel 71, 53121 Bonn, Germany

⁶ I. Physikalisches Institut der Universität zu Köln, Zùlpicher Strasse 77, 50937 Köln, Germany

⁷ The University of Arizona, Submillimeter Telescope Observatory, Tucson AZ 85721, USA

⁸ The University of Arizona, Steward Observatory, Tucson AZ 85721, USA

⁹ Instituto de Radioastronomia Milimétrica, Avenida Divina Pastora, 7NC, 18012 Granada, Spain

Received 1 October 1999 / Accepted 3 March 2000

Abstract. ^{12}CO $J = 1-0$, $2-1$, $4-3$, $7-6$, and ^{13}CO $1-0$, $2-1$, and $3-2$ line emission was mapped with angular resolutions of $13'' - 22''$ toward the nuclear region of the archetypical starburst galaxy M 82. There are two hotspots on either side of the dynamical center, with the south-western lobe being slightly more prominent. Lobe spacings are not identical for all transitions: For the submillimeter CO lines, the spacing is $\sim 15''$; for the millimeter lines (CO $J = 2-1$ and $1-0$) the spacing is $\sim 26''$, indicating the presence of a ‘low’ and a ‘high’ CO excitation component.

A Large Velocity Gradient (LVG) excitation analysis of the submillimeter lines leads to inconsistencies, since area and volume filling factors are almost the same, resulting in cloud sizes along the lines-of-sight that match the entire size of the M 82 starburst region. Nevertheless, LVG column densities agree with estimates derived from the dust emission in the far infrared and at submillimeter wavelengths. $22''$ beam averaged total column densities are $N(\text{CO}) \sim 5 \cdot 10^{18}$ and $N(\text{H}_2) \sim 10^{23} \text{ cm}^{-2}$; the total molecular mass is a few $10^8 M_{\odot}$.

Accounting for high UV fluxes and variations in kinetic temperature and assuming that the observed emission arises from photon dominated regions (PDRs) resolves the problems related to an LVG treatment of the radiative transfer. Spatial densities are as in the LVG case ($n(\text{H}_2) \sim 10^{3.7} \text{ cm}^{-3}$ and $\sim 10^3 \text{ cm}^{-3}$ for the high and low excitation component, respectively), but $^{12}\text{CO}/^{13}\text{CO}$ intensity ratios $\gtrsim 10$ indicate that the bulk of the CO emission arises in UV-illuminated diffuse cloud fragments of small column density ($N(\text{H}_2) \sim 5 \cdot 10^{20} \text{ cm}^{-2}/\text{km s}^{-1}$) and

sub-parsec cloud sizes with area filling factors $\gg 1$. Thus CO arises from quite a different gas component than the classical high density tracers (e.g. CS, HCN) that trace star formation rates more accurately. The dominance of such a diffuse molecular interclump medium also explains observed high [C I]/CO line intensity ratios. PDR models do not allow a determination of the relative abundances of ^{12}CO to ^{13}CO . Ignoring magnetic fields, the CO emitting gas appears to be close to the density limit for tidal disruption. Neither changes in the $^{12}\text{C}/^{13}\text{C}$ abundance ratio nor variations of the incident far-UV flux provide good fits to the data for simulations of larger clouds.

A warm diffuse ISM not only dominates the CO emission in the starburst region of M 82 but is also ubiquitous in the central region of our Galaxy, where tidal stress, cloud-cloud collisions, shocks, high gas pressure, and high stellar densities may all contribute to the formation of a highly fragmented molecular debris. ^{12}CO , $^{12}\text{CO}/^{13}\text{CO}$, and [C I]/CO line intensity ratios in NGC 253 (and NGC 4945) suggest that the CO emission from the centers of these galaxies arises in a physical environment that is similar to that in M 82. Starburst galaxies at large distances ($z \sim 2.2-4.7$) show ^{12}CO line intensity ratios that are consistent with those observed in M 82. PDR models should be applicable to all these sources. $^{12}\text{CO}/^{13}\text{CO}$ line intensity ratios $\gg 10$, sometimes observed in nearby ultraluminous mergers, require the presence of a particularly diffuse, extended molecular medium. Here [C I]/CO abundance ratios should be as large or even larger than in M 82 and NGC 253.

Key words: galaxies: active – galaxies: individual: M 82 – galaxies: ISM – galaxies: nuclei – galaxies: starburst – radio lines: galaxies

Send offprint requests to: C. Henkel (p220hen@mpifr-bonn.mpg.de)

* Based on observations with the Heinrich-Hertz-Telescope (HHT) and the IRAM 30-m telescope. The HHT is operated by the Submillimeter Telescope Observatory on behalf of Steward Observatory and the Max-Planck-Institut für Radioastronomie

1. Introduction

Low lying rotational transitions of CO are widely used as tracers of molecular hydrogen and are essential to determine dynamical properties and total molecular masses of galaxies. The widespread use of CO $J = 1-0$ and $2-1$ spectroscopy is however not sufficiently complemented by systematic surveys in higher rotational CO transitions to confine the excitation conditions of the dense interstellar medium (ISM). While the $J = 1$ and 2 states of CO are only 5.5 and 17 K above the ground level, the $J = 3$ to 7 states are at 33, 55, 83, 116, and 155 K and trace a component of higher excitation. ‘Critical densities’, at which collisional deexcitation matches spontaneous decay in the optically thin limit, are $\sim 10^{5-6} \text{ cm}^{-3}$ for CO $J = 3-2$ to $7-6$ in contrast to $10^{3.5}$ and $10^{4.3} \text{ cm}^{-3}$ for the ground rotational CO transitions.

Starburst galaxies are known to contain large amounts of molecular gas that may be heated to $T_{\text{kin}} \sim 100$ K by young massive stars, cosmic rays or turbulent heating. Therefore highly excited CO transitions, observed at submm-wavelengths, are the appropriate tool to study this interstellar gas component. Among the three nearest ($D \sim 3$ Mpc) nuclear starburst galaxies, NGC 253, NGC 4945, and M 82 (NGC 3034) M 82 is most readily accessible from telescopes of the northern hemisphere. Containing one of the brightest IRAS point sources beyond the Magellanic Clouds ($S_{100\mu\text{m}} \sim 1000$ Jy), M 82 has been observed at a variety of wavelengths, ranging from the radio to the γ -ray domain of the electromagnetic spectrum. The starburst in M 82 is likely triggered by a tidal interaction with M 81, causing a high infrared luminosity ($L_{\text{FIR}} \sim 4 \cdot 10^{10} L_{\odot}$), a high density of supernova remnants, and copious amounts of dense gas with strong OH and H₂O masers and a large number of molecular high density tracers (for CO maps, see Sutton et al. 1983; Olofsson & Rydbeck 1984; Young & Scoville 1984; Nakai et al. 1986, 1987; Lo et al. 1987; Loiseau et al. 1988, 1990; Phillips & Mampaso 1989; Turner et al. 1991; Tilanus et al. 1991; Sofue et al. 1992; White et al. 1994; Shen & Lo 1995; Kikumoto et al. 1998; Neininger et al. 1998).

So far, few CO $4-3$ maps of external galaxies were published (for M 51, M 82, M 83, and NGC 6946 see White et al. 1994; Petitpas & Wilson 1998; Nieten et al. 1999). Among these M 82 is the only true starburst galaxy but its CO $4-3$ map (White et al. 1994) is confined to the very central region. With respect to higher rotational CO transitions, only a few CO $6-5$ spectra were presented from nearby galaxies (Harris et al. 1991; Wild et al. 1992).

We have used the Heinrich-Hertz-Telescope (HHT) on Mt. Graham (Baars & Martin 1996) to map M 82 in the CO $J = 7-6$, $4-3$, and ^{13}CO $3-2$ transitions. These data are complemented by new $J = 2-1$ and $1-0$ spectra taken with the IRAM 30-m telescope.

2. Observations

2.1. Observations with the Heinrich-Hertz-Telescope

^{13}CO $3-2$ (331 GHz $\simeq 907\mu\text{m}$), ^{12}CO $4-3$ (461 GHz $\simeq 650\mu\text{m}$), and ^{12}CO $7-6$ (807 GHz $\simeq 372\mu\text{m}$) line emission was observed

at the HHT during Feb. 1999 with beamwidths of $\sim 22''$, $18''$, and $13''$, respectively. For the CO $3-2$ and $4-3$ transitions, SIS receivers were employed; the CO $7-6$ line was observed with a Hot Electron Bolometer (HEB) kindly provided by the Center for Astrophysics (Kawamura et al. 1999). The backends consisted of two acousto optical spectrometers, each with 2048 channels (channel spacing ~ 480 kHz, frequency resolution ~ 930 kHz) and a total bandwidth ~ 1 GHz.

Spectra were taken using a wobbling (2 Hz) secondary mirror with a beam throw of ± 120 to $\pm 240''$ in azimuth. Scans obtained with reference positions on either azimuth were coadded to ensure flat baselines. Receiver temperatures were at the order of 170 K at 331 GHz, 150 K at 461 GHz, and 1000 K at 807 GHz; system temperatures were ~ 900 , 3500, and 8000 K on a T_{A}^* scale, respectively.

The receivers were sensitive to both sidebands. Any imbalance in the gains of the lower and upper sideband would thus lead to calibration errors. To account for this, we have observed Orion-KL (at 807 GHz) and IRC+10216 (at 807 and 331 GHz) prior to our M 82 measurements with the same receiver tuning setup. Peak temperatures were 70, 20, and 2.3 K on a T_{A}^* scale, respectively (cf. Howe et al. 1993; Groesbeck et al. 1994). At 461 GHz, Orion-KL ($T_{\text{A}}^* \sim 70$ K; cf. Schulz et al. 1995) was mapped but the tuning was later changed by $\Delta V = 200 \text{ km s}^{-1}$ for M 82 (see Sect. 3.2).

All results displayed are given on a main beam brightness temperature scale (T_{mb}). This is related to T_{A}^* via $T_{\text{mb}} = T_{\text{A}}^* (F_{\text{eff}}/B_{\text{eff}})$ (see Downes 1989). Main beam efficiencies, B_{eff} , were 0.5, 0.38, and 0.36 at 330, 461, and 806 GHz, as obtained from measurements of Saturn. Forward hemisphere efficiencies are 0.9, 0.75, and 0.70, respectively (D. Muters, priv. comm.). With an rms surface accuracy of $\sim 20\mu\text{m}$ ($\lambda/18$ at 806 GHz), the HHT is quite accurate. This reduces the effect of the source coupling efficiency on the measured source size.

At the center of M 82, CO lineshapes depend sensitively on the position observed, so that in each of our maps the dynamical center could be identified with an accuracy better than $5''$. While relative pointing errors should be small when compared to the spacing ($10''$) of our ^{13}CO $J = 3-2$ and CO $4-3$ maps, relative pointing is less reliable in the case of the CO $J = 7-6$ map; here deviations may reach $\pm 5''$ for a few positions.

2.2. Observations with the IRAM 30-m telescope

^{12}CO and ^{13}CO $J = 1-0$ and $2-1$ observations were made with SIS receivers of high image sideband rejection (~ 25 db for $1-0$ and ~ 13 db for $2-1$ line data) of the inner $50'' \times 50''$ (^{12}CO ; $5''$ spacing for the central $20''$, otherwise $10''$) and $20'' \times 20''$ (^{13}CO ; $5''$ spacing) of M 82 in June 1999. The measurements were made in a position switching mode with the off-position displaced by $15'$ in right ascension. The two ^{12}CO lines (as well as those of ^{13}CO) were measured simultaneously. Beamwidths at 115 ($J = 1-0$) and 230 GHz ($J = 2-1$) were 21 and $13''$; forward hemisphere and beam efficiencies were 0.92 and 0.72 for the $J = 1-0$ and 0.89 and 0.45 for the $J = 2-1$ data, respectively. Calibration was checked by observing IRC+10216. Measured

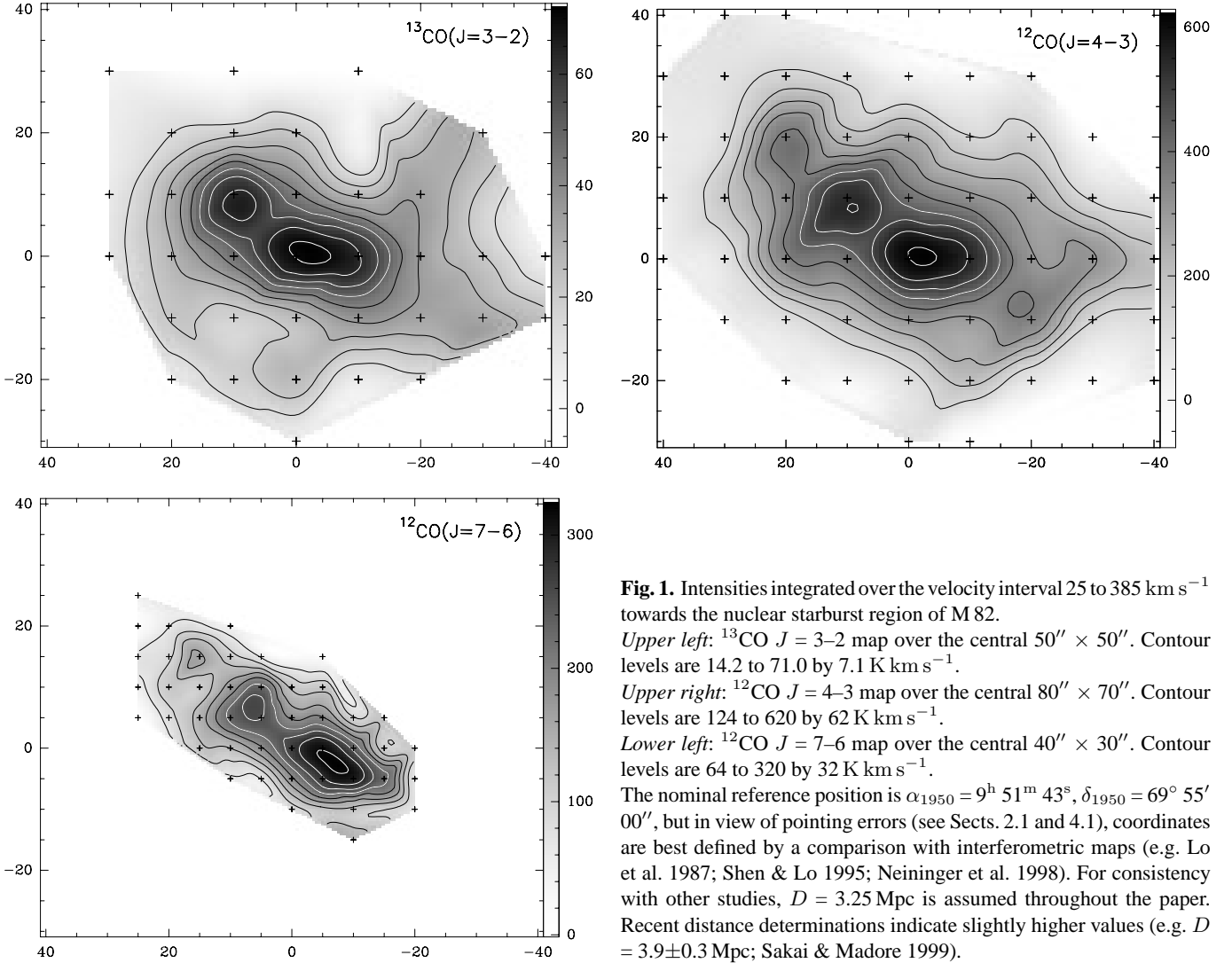


Fig. 1. Intensities integrated over the velocity interval 25 to 385 km s⁻¹ towards the nuclear starburst region of M 82.

Upper left: ¹³CO $J = 3-2$ map over the central 50'' \times 50''. Contour levels are 14.2 to 71.0 by 7.1 K km s⁻¹.

Upper right: ¹²CO $J = 4-3$ map over the central 80'' \times 70''. Contour levels are 124 to 620 by 62 K km s⁻¹.

Lower left: ¹²CO $J = 7-6$ map over the central 40'' \times 30''. Contour levels are 64 to 320 by 32 K km s⁻¹.

The nominal reference position is $\alpha_{1950} = 9^{\text{h}} 51^{\text{m}} 43^{\text{s}}$, $\delta_{1950} = 69^{\circ} 55' 00''$, but in view of pointing errors (see Sects. 2.1 and 4.1), coordinates are best defined by a comparison with interferometric maps (e.g. Lo et al. 1987; Shen & Lo 1995; Neininger et al. 1998). For consistency with other studies, $D = 3.25$ Mpc is assumed throughout the paper. Recent distance determinations indicate slightly higher values (e.g. $D = 3.9 \pm 0.3$ Mpc; Sakai & Madore 1999).

line intensities were $T_{\text{mb}} = 17$ and 43 K for ¹²CO $J = 1-0$ and 2-1 (channel spacings were 3.2 and 1.6 km s⁻¹, respectively) and 2.3 and 6.0 K for ¹³CO $J = 1-0$ and 2-1 (channel spacings: 2.7 and 1.4 km s⁻¹; cf. Mauersberger et al. 1989).

3. Results

3.1. Overall morphology of CO submillimeter line emission

Maps of integrated ¹³CO $J = 3-2$, ¹²CO 4-3, and ¹²CO 7-6 intensity are presented in Fig. 1. Detectable emission is strongly confined to the central part of the galaxy. In each map a particularly wide spectral feature, with slightly smaller peak intensity than the most intense lines in the SW and NE, could be identified with the dynamical center (see Fig. 2 which also contains IRAM spectra). Two main peaks of emission are detected, being displaced by almost 10'' from the center (this corresponds to a projected distance of 150 pc); the south-western hot spot is most prominent, while evidence for a third peak in the NE (at $\sim (17'', 17'')$), seen in the CO $J = 4-3$ and 7-6 maps, is not conclusive. Velocity channel maps of the ¹³CO $J = 3-2$ and

¹²CO $J = 4-3$ line emission are displayed in Fig. 3. These outline the extent of the emission at various velocities, show the dominant rotation pattern with the red-shifted lobe in the north-east and the blue-shifted lobe in the south-west, and indicate the rapid change in radial velocity near the dynamical center (cf. Neininger et al. 1998).

3.2. Consistency of CO line temperatures

Calibration at sub-millimeter wavelengths is critical because of rapidly changing weather conditions, high atmospheric opacities, imbalances in the receiver gains between the sidebands, and because of uncertainties in beam and forward hemisphere efficiencies. Calibration uncertainties introduced by these effects may rise up to $\pm 30\%$ and a comparison with data published elsewhere is needed. Intensities of our ¹³CO $J = 3-2$ spectra from the center, the south-western, and north-eastern lobes are smaller by $\sim 30\%$ than those given by Tilanus et al. (1991; their Fig. 3). Our spectrum from IRC+10216 is however 30% stronger (on a T_{mb} scale) than that given by Groesbeck et

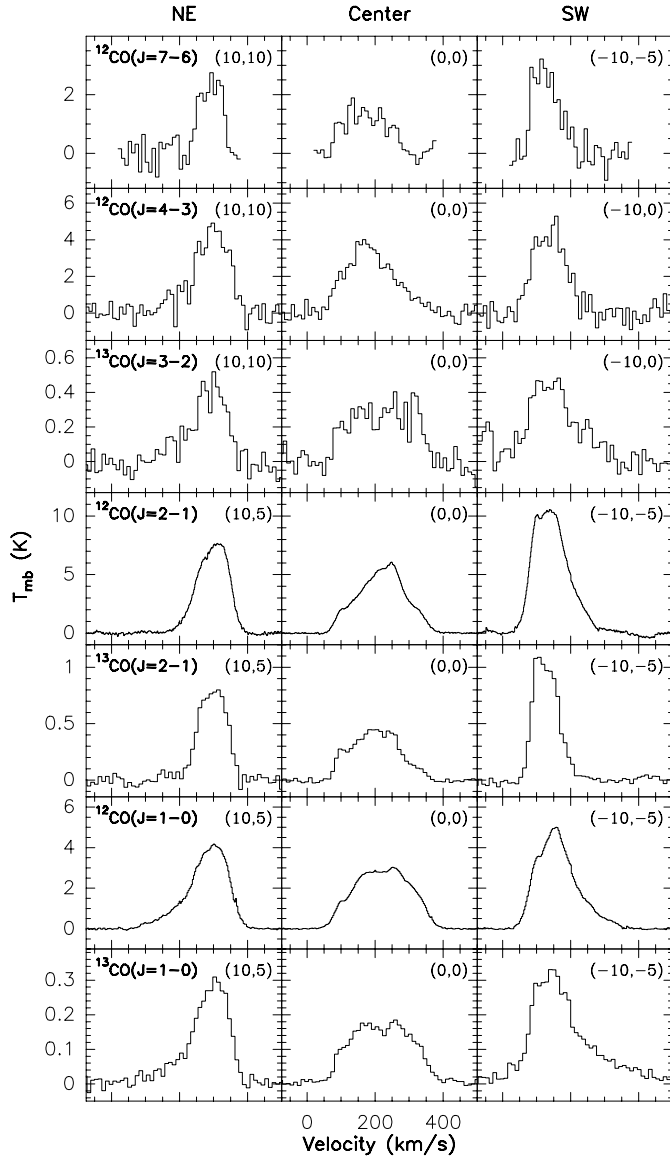


Fig. 2. Spectra towards the center (middle), the north-eastern (left), and the south-western (right) lobe. The temperature is given in units of main beam brightness temperature (K). Beamwidths are $13''$, $18''$, $22''$, $13''$, $13''$, $21''$ and $21''$ for the ^{12}CO 7–6, ^{12}CO 4–3, ^{13}CO 3–2, ^{12}CO and ^{13}CO 2–1, and ^{12}CO and ^{13}CO 1–0 profiles, respectively. Offsets in arcsec relative to a nominal center position (see Fig. 1) are given in the upper right corner of each box. Small differences in these offsets are caused by pointing deviations (Sect. 2) or changes in source morphology (Sect. 4). All data are smoothed to a channel width of $\sim 10 \text{ km s}^{-1}$. Linewidths (compare e.g. the $J = 2-1$ and $7-6$ profiles from the south-western lobe with the corresponding $J = 3-2$ and $1-0$ spectra) are affected by differences in beamsize.

al. (1994), so that our scaling is intermediate between those of Tilanus et al. and Groesbeck et al. $\text{CO } J = 4-3$ line intensities (Fig. 2) are $\sim 30\%$ larger than those given by White et al. (1994). Since their data were obtained with higher angular resolution (JCMT beamwidth: $11''$), this difference is significant. A comparison with the three $4-3$ spectra from the 10-m CSO shown

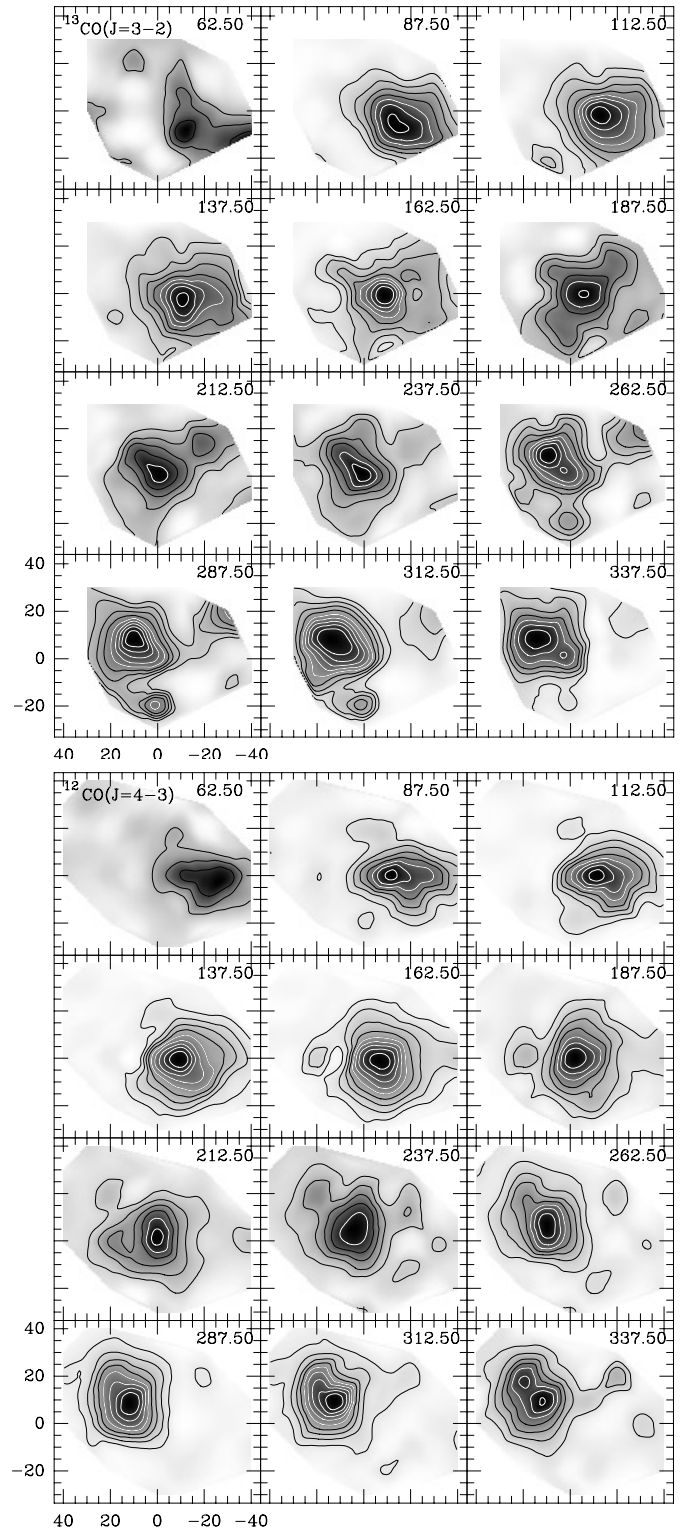


Fig. 3. $^{13}\text{CO } J = 3-2$ (upper panel) and $^{12}\text{CO } J = 4-3$ (lower panel) channel maps. Center velocities are given in the upper right corner of each box. The radial velocity range is 30 km s^{-1} per image. The lowest black contour, the lowest white contour and the interval are respectively 1.4 K km s^{-1} , 7 K km s^{-1} , and 1.4 K km s^{-1} (upper panel) and 14 K km s^{-1} , 70 K km s^{-1} , and 14 K km s^{-1} (lower panel) on a T_{mb} scale.

by Güsten et al. (1993) shows good agreement for the lobe positions. Differences in 4–3 peak temperatures between central and lobe positions are however less pronounced than reported by Güsten et al. (we find peak line temperature ratios of ~ 1.3 instead of ~ 2.0 between the lobes and the center). Our CO 7–6 line intensities from Orion-KL agree well with those obtained by Howe et al. (1993) with the 10-m CSO antenna.

Previous high angular resolution CO data from the 30-m telescope (compare Fig. 9a of Loiseau et al. 1990 with our Table 1) were affected by uncertainties in the image sideband ratios. Our new data are not significantly affected by this problem, should be reliably calibrated within $\pm 10\%$, and agree well with recent spectra obtained independently in an ‘on-the-fly’ observing mode (Weiß, in preparation).

3.3. Line intensity ratios

Claims that the large scale ($\gtrsim 20''$) integrated CO $J = 2-1/1-0$ line intensity ratio were much larger than unity (e.g. Knapp et al. 1980; Olofsson & Rydbeck 1984; Loiseau et al. 1990) can be firmly rejected. The more recently measured ratios of 1.0 (Wild et al. 1992), 1.1 (Mauersberger et al. 1999), and 1.0–1.4 (Table 1) imply that ^{12}CO line intensities of the three lowest rotational CO transitions must be similar over the central $22''$. Our ^{13}CO $J = 3-2$ line temperatures are a factor of ~ 10 smaller than those of the $J = 3-2$ ^{12}CO transition observed with the same telescope (R. Wielebinski, priv. comm.). The situation with respect to the $J = 6-5$ line remains unclear. 6–5 spectra from the western lobe (Harris et al. 1991) and the center (Wild et al. 1992; their Fig. 2) do not allow a beam convolution to the angular resolution of the lower frequency data and the beam pattern appears to be complex. Our $J = 7-6$ data show peak line temperatures of order 2–3 K. This is smaller than the 4 K measured in the $J = 4-3$ and lower J transitions with larger beam sizes. Beyond $J = 4-3$ we thus find *clear evidence for a weakening of CO emission with increasing rotational quantum number J .*

4. Spatial distributions: are there differences?

4.1. CO

A comparison of the CO $J = 4-3$ data presented in Fig. 1 with those of White et al. (1994) shows a strong discrepancy in the overall spatial distribution: Our CO $J = 4-3$ map contains (at least) two maxima of emission, while the higher angular resolution data of White et al. (1994) have only one peak. Data with only one peak (that are based on spectra with sufficient resolution to separate the lobes) are also presented by Wild et al. (1992; their Fig. 10 and Table 5) for ^{13}CO and C^{18}O $J = 2-1$. The original ^{13}CO $J = 2-1$ spectra displayed by Loiseau et al. (1988; their Fig. 1), however, clearly show a double-lobed distribution. Maps in the low- J ^{12}CO and ^{13}CO transitions (e.g. Lo et al. 1987; Nakai et al. 1987; Loiseau et al. 1988, 1990; Tilanus et al. 1991; Shen & Lo 1995; Neininger et al. 1998) as well as our $J = 7-6$ (Fig. 3), 2–1 and 1–0 data *all* show a double-lobed structure. We thus conclude that, in spite of previous evidence

to the contrary, *the overall spatial distribution of emission from highly excited CO shows two main centers of emission.*

Are the two main hotspots observed in the $J = 1-0$ and 2–1 transitions identical with those observed in higher excited CO lines? The position angles (east of north) of the lines connecting the hotspots are slightly smaller in our submillimeter data (Fig. 1) than in interferometric maps (cf. Lo et al. 1987; Shen & Lo 1995; Kikumoto et al. 1987; Neininger et al. 1998). This is likely an error in our data caused by measurements at varying hour angles with pointing offsets along the azimuth and elevation axes.

More significant is a *difference in angular separation*: While the two main peaks of line emission observed by us are separated by $15'' \pm 2''$, the interferometric maps (Lo et al. 1987; Shen & Lo 1995; Neininger et al. 1998) show a separation of $27'' \pm 2''$. This difference is larger than the positional uncertainties. A larger separation in the low- J transitions is also supported by filled-aperture measurements of Nakai et al. (1986, 1987) and Wild et al. (1992) for CO $J = 1-0$, by Loiseau et al. (1990) for CO $J = 2-1$, by Loiseau et al. (1988) for ^{13}CO $J = 2-1$, and by us for the ^{12}CO $J = 1-0$ and 2–1 lines. The CO $J = 3-2$ distribution (Tilanus et al. 1991) shows an intermediate lobe separation.

Which peaks are detected in the CO submillimeter lines? The two main lobes of CO emission are located almost symmetrically with respect to the kinematical center, both in lines of low (e.g. Neininger et al. 1998) and high (see Fig. 3) excitation. We can therefore exclude that we see the north-eastern lobe and the ‘compact central core’ (see Shen & Lo 1995; Neininger et al. 1998) that are separated by $\sim 15''$. Instead, *the sudden drop of angular separation from $27''$ to $15''$ must reveal inhomogeneities in the molecular ring that are characterized by changes in density and temperature.* In addition to the ‘high CO excitation component’ there exists a ‘low CO excitation component’, mainly emitting in the CO $J = 1-0$ and 2–1 lines. The transition in lobe separation occurs at the $J = 3-2$ line: In CO $J = 3-2$ (Tilanus et al. 1991) the separation is still $\sim 20''$. ^{13}CO $J = 3-2$ emission with smaller optical depths and less photon trapping requires, however, higher excited gas so that the lobe separation becomes smaller.

Since lobe separations are often comparable to the angular resolution of the particular observation, integrated intensity maps may be misleading as they easily exhibit structure dominated by the superposition of components with identical lines of sight but different velocities. To clarify the situation, we thus present in Fig. 4 position-velocity maps of the CO $J = 4-3$ (our HHT map with highest signal-to-noise ratio and best relative pointing) and CO 2–1 (Weiß, in preparation) line emission. Beam widths are $18''$ and $13''$, respectively. Surprisingly, *the p - v diagrams do not reproduce the strikingly different lobe separations seen in the integrated intensity maps.* This also holds when comparing CO $J = 2-1$ with 7–6 emission. *This hints at wider line profiles for the higher excited CO transitions at the inner edges of the CO $J = 1-0$ and 2–1 lobes.* This is corroborated by Fig. 4 that shows, for the CO $J = 4-3$ line, a slightly smaller lobe separation *and* a significantly larger full-width-to-half-power line width towards the inner edge of the south-western lobe.

Table 1. Line intensities ($T = T_{\text{mb}}$), integrated line intensities ($I = \int T_{\text{mb}} dv$), and line temperature ratios for a beamwidth of $22''$ ^a. CO $J = 1-0$ and $2-1$ data were obtained with the IRAM 30-m telescope, higher excited rotational lines were measured with the HHT.

Line or Line Ratio		Position ^b		
		NE-Lobe	Center	SW-Lobe
<i>Line temperatures:</i>				
$T(\text{CO } J = 7-6)$	(K)	1.08 ± 0.11	0.82 ± 0.11	1.37 ± 0.11
$T(\text{CO } J = 4-3)$	(K)	3.40 ± 0.18	2.82 ± 0.18	3.72 ± 0.18
$T(\text{CO } J = 2-1)$	(K)	4.16 ± 0.03	4.26 ± 0.04	5.33 ± 0.03
$T(\text{CO } J = 1-0)$	(K)	4.18 ± 0.03	3.14 ± 0.02	5.00 ± 0.03
$T(^{13}\text{CO } J = 3-2)$	(K)	0.40 ± 0.03	0.28 ± 0.03	0.41 ± 0.03
$T(^{13}\text{CO } J = 2-1)^c$	(K)	0.46 ± 0.02	0.31 ± 0.02	0.58 ± 0.02
$T(^{13}\text{CO } J = 1-0)$	(K)	0.30 ± 0.02	0.19 ± 0.01	0.30 ± 0.02
<i>Integrated Intensities:</i>				
$I(\text{CO } J = 7-6)$	(K km s ⁻¹)	132.3 ± 5.8	177.7 ± 5.4	167.2 ± 6.4
$I(\text{CO } J = 4-3)$	(K km s ⁻¹)	465.3 ± 12.9	493.3 ± 12.1	503.0 ± 12.6
$I(\text{CO } J = 2-1)$	(K km s ⁻¹)	674.3 ± 0.8	847.9 ± 1.2	804.9 ± 1.1
$I(\text{CO } J = 1-0)$	(K km s ⁻¹)	573.9 ± 0.6	663.0 ± 0.6	672.8 ± 0.8
$I(^{13}\text{CO } J = 3-2)$	(K km s ⁻¹)	51.2 ± 4.9	71.7 ± 3.8	68.0 ± 2.8
$I(^{13}\text{CO } J = 2-1)^c$	(K km s ⁻¹)	58.9 ± 1.1	59.8 ± 0.9	69.0 ± 1.1
$I(^{13}\text{CO } J = 1-0)$	(K km s ⁻¹)	40.1 ± 0.5	41.6 ± 0.3	58.8 ± 0.6
<i>Ratios:</i>				
$T(\text{CO } J = 7-6/\text{CO } J = 4-3)$		0.32 ± 0.03	0.29 ± 0.04	0.37 ± 0.03
$T(\text{CO } J = 4-3/^{13}\text{CO } J = 3-2)$		8.50 ± 0.87	10.1 ± 1.26	9.07 ± 0.80
$T(\text{CO } J = 2-1/\text{CO } J = 1-0)$		1.00 ± 0.01	1.36 ± 0.02	1.07 ± 0.01
$T(^{13}\text{CO } J = 3-2/^{13}\text{CO } J = 2-1)^c$		0.87 ± 0.08	0.90 ± 0.11	0.71 ± 0.06
$T(^{13}\text{CO } J = 2-1/^{13}\text{CO } J = 1-0)^c$		1.53 ± 0.08	1.63 ± 0.06	1.93 ± 0.04
$T(\text{CO } J = 2-1/^{13}\text{CO } J = 2-1)^c$		9.04 ± 0.40	13.7 ± 0.90	9.19 ± 0.32
$T(\text{CO } J = 1-0/^{13}\text{CO } J = 1-0)^c$		13.9 ± 0.93	16.5 ± 0.88	16.7 ± 1.12
$I(\text{CO } J = 7-6/\text{CO } J = 4-3)$		0.28 ± 0.01	0.36 ± 0.01	0.33 ± 0.02
$I(\text{CO } J = 4-3/^{13}\text{CO } J = 3-2)$		9.09 ± 0.91	6.88 ± 0.40	7.40 ± 0.36
$I(\text{CO } J = 2-1/\text{CO } J = 1-0)$		1.17 ± 0.01	1.28 ± 0.01	1.20 ± 0.01
$I(^{13}\text{CO } J = 3-2/^{13}\text{CO } J = 2-1)^c$		0.87 ± 0.08	1.20 ± 0.06	0.99 ± 0.04
$I(^{13}\text{CO } J = 2-1/^{13}\text{CO } J = 1-0)^c$		1.47 ± 0.03	1.44 ± 0.02	1.17 ± 0.02
$I(\text{CO } J = 2-1/^{13}\text{CO } J = 2-1)^c$		11.4 ± 0.21	14.2 ± 0.21	11.7 ± 0.19
$I(\text{CO } J = 1-0/^{13}\text{CO } J = 1-0)^c$		14.3 ± 0.18	15.9 ± 0.12	11.4 ± 0.12

^a Given 1σ errors in T_{mb} and $\int T_{\text{mb}} dv$ were determined from gaussian fits and neither include calibration uncertainties (see Sects. 2 and 3.2) nor errors caused by the limited spatial coverage of our CO 7–6 (Fig. 1), $^{13}\text{CO } 2-1$, and $^{13}\text{CO } 1-0$ (Sect. 2) maps. For the beam convolution, gaussian distributions were assumed for the telescope beam and the source. While all measured positions were taken for beam convolution, the CO $J = 4-3$ beam size is almost as large as that for the $^{13}\text{CO } J = 3-2$ spectra. Therefore only five measured CO $J = 4-3$ spectra, the profile measured toward the specific position and those with offsets of $10''$ along the four cardinal directions, dominate the convolution. For the $J = 7-6$ line, spatially constraining the convolution to positions with weights >0.3 or $\Delta = 11''/7$ (weight = $\exp[-4 \ln 2 (\Delta^2/(\theta_{b1}^2 - \theta_{b2}^2))]$; Δ : Offset; $\theta_{b1} = 22''$, $\theta_{b2} = 18''$ or $13''$ for $J = 4-3$ and $7-6$ spectra, respectively) modifies the result by only $\sim 5\%$.

^b For the offsets in arcsec, see Fig. 2.

^c Because of the limited extent of the $^{13}\text{CO } J = 2-1$ map (Sect. 2.2), $^{13}\text{CO } 2-1$ values for the lobes should be considered with caution. The problem is less severe for the $^{13}\text{CO } J = 1-0$ transition, because beam convolution is not required in this case.

4.2. Other tracers of the interstellar medium

Table 2 displays lobe separations determined by various tracers of atomic line, molecular line, or dust continuum emission. There are three preferred angular distances: $\sim 26''$, $15''$, and $10''$. Spectral lines of low excitation show two maxima at an angular distance of $\sim 26''$. Highly excited lines and the far-infrared and mm-wave continuum show a lobe separation of $\sim 15''$. The continuum in the near and mid infrared and the Br γ line show an angular spacing of $\sim 10''$.

Since the dynamical center of the galaxy is located not too far from the mid point of the line connecting the lobes, these data show evidence for an even more complex structure than indicated by the CO data alone. The hot dust and Br γ emission from the inner parts of the ring may trace the most recent star formation activity as it propagates outwards into the molecular lobes located at larger galactocentric distances (Alton et al. 1999).

Table 2. Lobe separations^a

Tracer	Separation arcsec	Reference
<i>Continuum</i>		
2.2 μ m	9 \pm 1	McLeod et al. (1993) ^b
2.2 μ m	8 \pm 2	Dietz et al. (1986)
10.0 μ m	9 \pm 1	Dietz et al. (1989)
10.8 μ m	9 \pm 1	Telesco et al. (1991)
12.4 μ m	9 \pm 1	Telesco & Gezari (1992)
19.2 μ m	11 \pm 2	Telesco et al. (1991)
19.5 μ m	10 \pm 2	Dietz et al. (1989)
30.0 μ m	10 \pm 2	Telesco et al. (1991)
450 μ m	16 \pm 2	Alton et al. (1999)
450 μ m	16 \pm 3	Smith et al. (1991)
450 μ m	14 \pm 1	Hughes et al. (1994)
850 μ m	16 \pm 2	Alton et al. (1999)
1300 μ m	18 \pm 4	Krügel et al. (1990)
2700 μ m	17 \pm 2	Neininger et al. (1998)
3400 μ m	18 \pm 4	Seaquist et al. (1998)
<i>Spectral lines^c</i>		
Br γ 2.16 μ m	10 \pm 2	Lester et al. (1990)
Br γ 2.16 μ m	10 \pm 2	Larkin et al. (1994)
[Ne II] 12.8 μ m	15 \pm 1	A & L (1995) ^d
CO 7–6 0.37 mm	15 \pm 3	This paper
[C I] 0.6 mm	21 \pm 6	White et al. (1994) ^e
CO 4–3 0.65 mm	14 \pm 3	This paper
CO 3–2 0.9 mm	20 \pm 5	Tilanus et al. (1991)
¹³ CO 3–2 0.9 mm	13 \pm 3	This paper
CO 2–1 1.3 mm	24 \pm 3	Loiseau et al. (1990)
¹³ CO 2–1 1.4 mm ^f	15 \pm 5	Loiseau et al. (1988)
CO 1–0 2.6 mm	26 \pm 2	Shen & Lo (1995)
CO 1–0 2.6 mm	25 \pm 3	Carlstrom (1988)
CO 1–0 2.6 mm	27 \pm 3	Lo et al. (1987)
CO 1–0 2.6 mm	16 \pm 5	Nakai et al. (1987)
¹³ CO 1–0 2.7 mm	27 \pm 2	Neininger et al. (1998)
CS 2–1 3.1 mm	26 \pm 3	Baan et al. (1990)
HCO ⁺ 1–0 3.4 mm ^g	20 \pm 2	Carlstrom (1988)
HCN 1–0 3.4 mm	24 \pm 3	Carlstrom (1988)
HI 21 cm	29 \pm 3	Weliachew et al. (1984)

^a Errors are mainly by-eye-estimates.

^b From Fig. 10 of McLeod et al. (1993)

^c Lobe separations refer to maps displaying integrated line intensities.

^d Achtermann & Lacey (1995)

^e Since the CO $J = 4-3$ map of White et al. (1994) lacks the characteristic double lobed structure, their [C I] 492 GHz map should also be confirmed by independent measurements.

^f The given lobe separation refers to Fig. 2 of Loiseau et al. (1988), displaying integrated line intensities. Peak line temperatures (their Fig. 1) show a separation of $\sim 25''$.

^g The interferometric HCO⁺ map of Carlstrom (1988; angular resolution: $10''$) shows two pronounced peaks. It is however difficult to identify the lobes in the integrated intensity map of Seaquist et al. (1998; angular resolution $3''.50 \times 3''.25$). This may be caused by missing flux in the latter map.

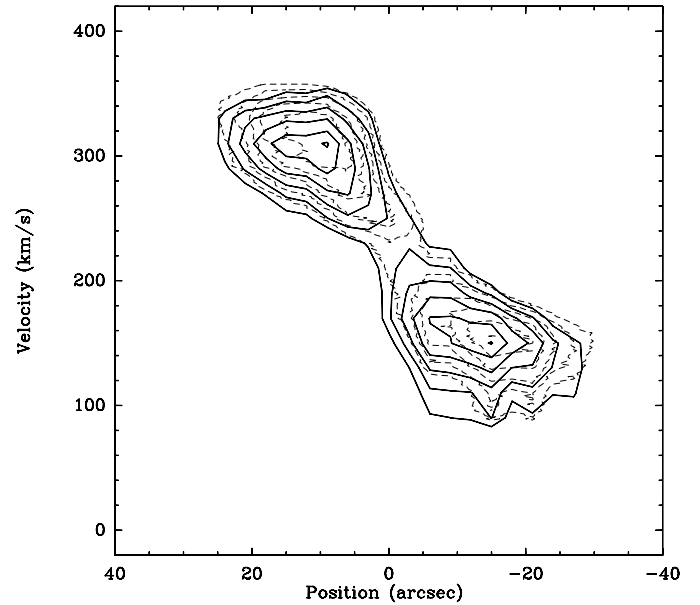


Fig. 4. Position-velocity diagram for CO $J = 4-3$ (solid lines; our data) and $2-1$ (dashed lines; data from Weiß (in preparation)) along the line connecting the south-western and north-eastern lobe. Angular resolutions are $18''$ and $13''$, respectively. The zero offset position is located half way between the emission peaks. CO contour levels are 50%, 60%, ..., 90%, and 99% of the respective peak intensities (see Table 1).

Since the far infrared and submillimeter continuum are associated with the central portion of the ring, this is the location where column densities of the cool dense gas must be largest.

5. Excitation analysis

The $J = 7-6$ transition is the CO line with highest rotational quantum number so far observed in M 82. Measurements of this line widen the range of excitation accessible by CO data considerably. To analyse these excitation conditions, we have performed radiative transfer calculations using a Large Velocity Gradient (LVG) model describing a cloud of spherical geometry (see Appendix A).

5.1. Physical parameters: our data

The three submillimeter CO transitions measured by us arise from the *high excitation component*, show a similar spatial distribution, and can therefore be used simultaneously in a radiative transfer analysis. To obtain true line intensity ratios, the CO 4–3 and 7–6 spectra were smoothed to the angular resolution of the ¹³CO 3–2 data. Table 1 displays these ratios for a beamwidth of $22''$, assuming gaussian beamshapes. As indicated by the spatial distributions (see Fig. 1), line ratios are similar toward the lobes and the central beam. CO 7–6/4–3 (integrated) line intensity ratios are at the order of 0.3, while ¹²CO 4–3/¹³CO 3–2 ratios are 7 – 10 (see Table 1).

In Appendix A (Fig. A.1) we plot our LVG line intensity ratios as a function of density, kinetic temperature, ¹²CO/¹³CO ratio, and CO ‘abundance’ (i.e., $X(\text{CO})/\text{grad } V$

Table 3. LVG model parameters (compare with Table 4)

		Footnote
<i>High excitation comp.</i>		
$^{12}\text{CO}/^{13}\text{CO}$	50–75	a
T_{kin}	60–130 K	
$n(\text{H}_2)$	$10^{3.3\dots3.9} \text{ cm}^{-3}$	
$f_{a,22''}$	0.04... 0.07	b
$f_{a,15''}$	0.07... 0.11	b
$f_{v,22''}$	~ 0.05	c
$\tau(\text{CO } J = 1-0)$	0.5 – 4.5	
$\tau(\text{CO } J = 2-1)$	3.5 – 15	
$\tau(\text{CO } J = 4-3)$	10 – 40	
$\tau(\text{CO } J = 7-6)$	6 – 25	
$N(\text{CO})_{22''}$	$\sim 5 \cdot 10^{18} \text{ cm}^{-2}$	d
$N(\text{H}_2)_{22''}$	$\sim 10^{23} \text{ cm}^{-2}$	d
$N(\text{CO})_{\text{cloud}}$	$\sim 10^{20} \text{ cm}^{-2}$	e
$N(\text{H}_2)_{\text{cloud}}$	$\sim 10^{24\dots25} \text{ cm}^{-2}$	e
	$\sim 10^{22} \text{ cm}^{-2}/\text{km s}^{-1}$	
$\langle n(\text{H}_2) \rangle_{22''}$	$\sim 200 \text{ cm}^{-3}$	
r_{cloud}	$\sim 150 \text{ pc}$	f
$M_{\text{mol},22''}$	$\sim 1-7 \cdot 10^8 M_{\odot}$	
<i>Low excitation comp.</i>		
$n(\text{H}_2)$	$\sim 10^3 \text{ cm}^{-3}$	

^a Abundance ratio

^b $f_{a,22''}$: Area filling factor for the central 22''

^c $f_{v,22''}$: Volume filling factor for the central 22''

^d $N(\text{CO})_{22''}$, $N(\text{H}_2)_{22''}$: 22'' beam averaged total column densities

^e $N(\text{CO})_{\text{cloud}}$, $N(\text{H}_2)_{\text{cloud}}$: 22'' cloud averaged total column densities

^f r_{cloud} : Characteristic molecular cloud size

with $X(\text{CO}) = [\text{CO}]/[\text{H}_2]$. For the line parameters given in Table 1, reasonable solutions can be found for small CO abundances ($X(\text{CO})/\text{grad } V \sim 10^{-6} \text{ pc}/\text{km s}^{-1}$) and high $^{12}\text{CO}/^{13}\text{CO}$ ratios (~ 75). High CO abundances ($X(\text{CO})/\text{grad } V \sim 10^{-3} \text{ pc}/\text{km s}^{-1}$) and small $^{12}\text{CO}/^{13}\text{CO}$ ratios are however not providing a realistic solution, because H_2 densities would approach 10^2 cm^{-3} and would thus become prohibitively small. Calculations assuming a plane-parallel instead of a spherical cloud geometry would yield even smaller densities.

A comparison of linewidths and velocity drifts with the size of the region suggests $\text{grad } V \sim 1 \text{ km s}^{-1}/\text{pc}$. With this value and $X(\text{CO}) \sim 10^{-5} - 10^{-4}$ (e.g. Blake et al. 1987; Farquhar et al. 1994) we can exclude a $^{12}\text{CO}/^{13}\text{CO}$ abundance ratio as small as 25 and are guided to the four diagrams of Fig. A.1 with $\log X(\text{CO}) \sim \log (X(\text{CO})/[\text{grad } V/\text{km s}^{-1} \text{ pc}^{-1}]) = -5$ or -4 and $^{12}\text{CO}/^{13}\text{CO} = 50$ or 75 . Our parameters are summarized in Table 3. Kinetic temperatures are $T_{\text{kin}} \sim 60 - 130 \text{ K}$, densities $n(\text{H}_2) \sim 10^{3.3-3.9} \text{ cm}^{-3}$, and area filling factors $f_{a,22''} \sim 0.04 - 0.07$ and $f_{a,15''} \sim 0.07 - 0.11$. While the density is well constrained, the kinetic temperature is less well determined. Solutions with $T_{\text{kin}} \gtrsim 150 \text{ K}$ are however unlikely because they would require H_2 densities $\lesssim 10^3 \text{ cm}^{-3}$. Even excluding such extreme solutions, the density of the CO emitting gas is small when compared with that of the Orion Hot Core (e.g. Schulz et al. 1995; van Dishoeck & Blake

1998), but *column densities* are large: With $N(\text{CO}) = 3.08 \cdot 10^{18} [n_{\text{CO}}/\text{cm}^{-3}] [(\Delta V/\text{grad } V)/\text{pc}] \text{ cm}^{-2}$, we obtain the 22'' beam averaged and cloud averaged column densities displayed in Table 3. For a line-of-sight source size of 350 pc and $N(\text{H}_2)_{22''} = 10^{23} \text{ cm}^{-2}$ (see Table 3), the beam averaged mean molecular density is $\langle n(\text{H}_2) \rangle_{22''} \sim 200 \text{ cm}^{-3}$ and the volume filling factor becomes $f_{v,22''} = \langle n(\text{H}_2) \rangle_{22''}/n(\text{H}_2) \sim 0.05$. Since the ratio $f_{v,22''}/f_{a,22''}$ denotes the line of sight dimension of the clouds in units of the beam size, we obtain with $r_{\text{cloud}} = 0.5 \text{ tg } 22'' D_{\text{pc}} [f_{v,22''}/f_{a,22''}] \sim 150 \text{ pc}$ a characteristic cloud radius (that will be discussed and revised in Sects. 6.2 and 6.3). The total molecular mass is $M_{\text{mol},22''} \sim 1-7 \cdot 10^8 M_{\odot}$.

5.2. Physical parameters: all CO data

So far, we have only analysed the ‘warm CO component’ of M 82, exclusively seen in $^{13}\text{CO } J = 3-2$ and higher excited rotational transitions. To combine these results with data from lower J rotational transitions and to further elucidate the physical state of the gas, Figs. 5–7 show (integrated) line intensities as a function of quantum number J . Calibration errors are at the order of $\pm 10\%$ in the $J = 1-0$ and $2-1$ lines and $\pm 20\%$ in the higher excited lines.

Figs. 5 and 6 show (integrated) line temperatures for a 22'' beam toward the dynamical center of the galaxy. Fig. 7 displays line temperatures for a 15'' beam toward the lobes and demonstrates that CO excitation is similar toward the south-western and north-eastern hotspot. Results from radiative transfer calculations (see Sect. 5.1 and Appendix A) are also given. Input parameters correspond to the four boxes in Fig. A.1 that provide a promising fit to the data ($\log (X(\text{CO})/[\text{grad } V/\text{km s}^{-1} \text{ pc}^{-1}]) = -5$ or -4 and $^{12}\text{CO}/^{13}\text{CO} = 50$ or 75).

Apparently there is a problem with the CO $J = 4-3$ line: The integrated intensity (Fig. 6) does not allow a reasonable fit, while the peak intensity (Fig. 5) is ‘appropriate’. This is caused by the narrow lineshape of our 4–3 spectrum (Fig. 2). Compared with other lines, the integrated line intensity is too small, but the peak line temperature is almost ‘normal’. The CO $J = 4-3$ profile, shown by Güsten et al. (1993) for the central position, is also weak, both with respect to its peak and integrated line intensity. The emission from the lobes, however, fits into the general trend (Fig. 7). An interpretation in terms of a diminished lobe separation for CO $J \geq 4-3$ (see Sect. 4.1) is not conclusive: The 22'' beam centered on the dynamical core of M 82 is mainly confined to the inner parts of the lobes and should not be greatly affected by emission from further out. A CO $J = 4-3$ deficiency is neither seen in Fig. 7 nor in a corresponding plot showing integrated intensities for a 15'' beam.

To summarize: Data from the $J = 4-3$ line are contradictory so that convincing evidence for a true anomaly is missing. In spite of differences in lobe separation (Sect. 4.1), the CO data can be reproduced, within observational errors, with densities, temperatures, filling factors, $[\text{CO}]/[\text{H}_2]$ abundances, and $^{12}\text{CO}/^{13}\text{CO}$ isotope ratios deduced from the three submillimeter transitions mapped by us with the HHT (Fig. 1).

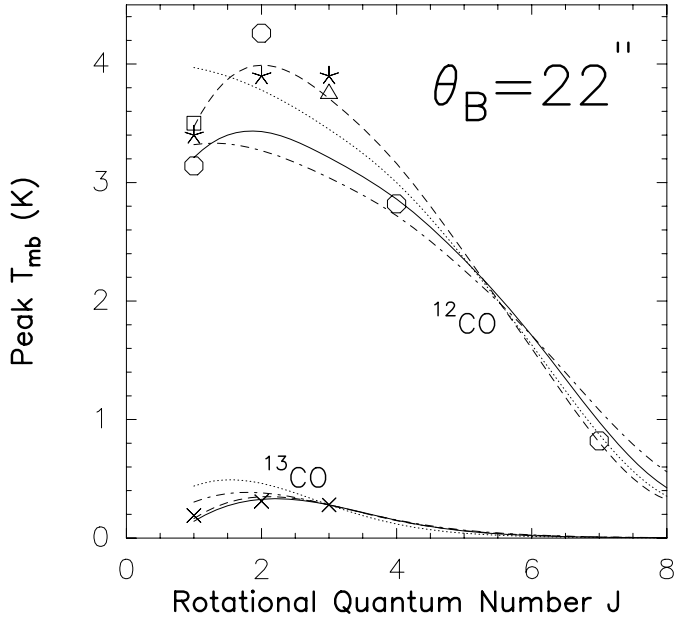


Fig. 5. Peak line temperatures as a function of rotational quantum number J ($J \rightarrow J - 1$) for a beam size of $22''$ toward the dynamical center of M 82. ^{12}CO : Open square: Wild et al. (1992); stars: Mauersberger et al. (1999); open triangle: R. Wielebinski (priv. comm.); circles: this paper. ^{13}CO (crosses): this paper. Results from radiative transfer calculations are given for ^{12}CO and ^{13}CO . Solid lines: $X(\text{CO})/\text{grad } V = 10^{-5}$ and $1.33 \cdot 10^{-7} \text{ pc/km s}^{-1}$, $n(\text{H}_2) = 8000 \text{ cm}^{-3}$, $T_{kin} = 70 \text{ K}$; dashed lines: $X(\text{CO})/\text{grad } V = 10^{-5}$ and $2 \cdot 10^{-7} \text{ pc/km s}^{-1}$, $n(\text{H}_2) = 5000 \text{ cm}^{-3}$, $T_{kin} = 100 \text{ K}$; dotted lines: $X(\text{CO})/\text{grad } V = 10^{-4}$ and $1.33 \cdot 10^{-6} \text{ pc/km s}^{-1}$, $n(\text{H}_2) = 2000 \text{ cm}^{-3}$, $T_{kin} = 80 \text{ K}$; dash-dotted lines: $X(\text{CO})/\text{grad } V = 10^{-4}$ and $2 \cdot 10^{-6} \text{ pc/km s}^{-1}$, $n(\text{H}_2) = 2000 \text{ cm}^{-3}$, $T_{kin} = 130 \text{ K}$.

There are few constraints for the *low excitation component* that is mainly seen in the CO $J = 1-0$ and $2-1$ lines. The column density must be smaller than for the high excitation component because the latter is more closely related to the far infrared and submillimeter continuum from the dust (Sect. 4.2). In view of the remarkable number of ‘super’-star clusters (O’Connell et al. 1995) and supernovae (Kronberg et al. 1985) near the outer portions of the ring, cloud temperatures for the low excitation component should also be $T_{kin} \gg 10 \text{ K}$. For $T_{kin} \sim 50 \text{ K}$, LVG densities are at the order of $n(\text{H}_2) \sim 10^3 \text{ cm}^{-3}$ or less.

6. Discussion

6.1. A comparison with other LVG simulations

The most detailed models of CO emission from M 82 were so far provided by Güsten et al. (1993). In order to fit the $^{12}\text{CO}/^{13}\text{CO}$ $J = 1-0$ and $2-1$ line intensity ratios then available, they rejected a one component LVG scenario and introduced two gas components, one of low ($n(\text{H}_2) \sim 10^3 \text{ cm}^{-3}$) and one of high ($\sim 10^5 \text{ cm}^{-3}$) density. The low density component is similar to that proposed by us for the gas mainly emitting in the CO $J = 1-0$ and $2-1$ lines (see Sect. 4.1). Our parameters for the high

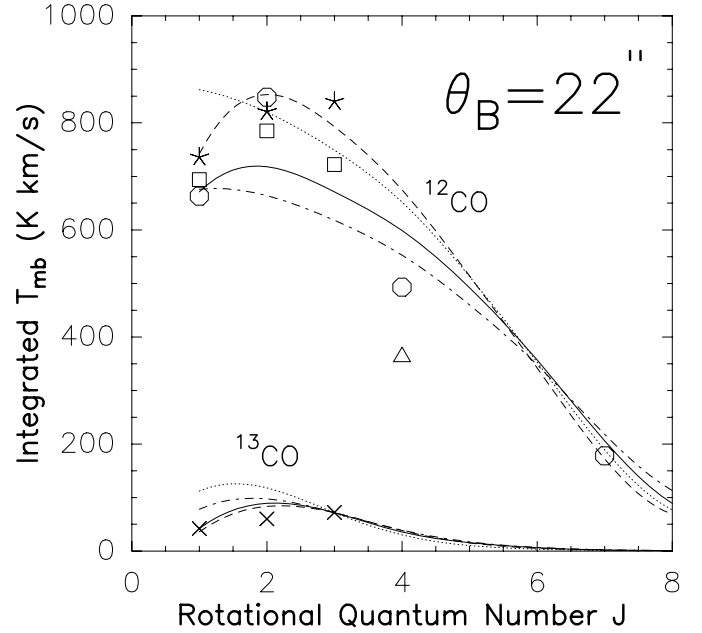


Fig. 6. Integrated line intensities as a function of rotational quantum number J ($J \rightarrow J - 1$) for a beam size of $22''$ toward the dynamical center of M 82. ^{12}CO : Open squares: Wild et al. (1992); open triangle: Güsten et al. (1993); stars: Mauersberger et al. (1999); circles: this paper. ^{13}CO (crosses): this paper. While most of our spatially convolved integrated line intensities were obtained from relatively extended maps (see Fig. 1), the convolution of our ^{13}CO $J = 2-1$ data may be affected by insufficient spatial coverage (see Sect. 2.2). The CO $J = 2-1$, $3-2$, and $4-3$ data from Wild et al. (1992) and Güsten et al. (1993) are based on few observed positions only. These cover the ridge of strong CO emission and only allow to estimate intensities for the dynamical center of M 82. To account for the missing positions, the resulting integrated intensities were multiplied by 0.85 (the factor was deduced from the CO $J = 3-2$ map of Tilanus et al. 1991). Results from radiative transfer calculations are also given (for the parameters, see Fig. 5).

CO excitation component agree to a large extent with those of the one component scenario of Güsten et al. (1993).

For the highly excited gas we thus also find optically thick ^{12}CO low- J emission and a high $[^{12}\text{CO}]/[^{13}\text{CO}]$ abundance ratio ($\gtrsim 50$; see Table 3), that is further supported by an independent chain of arguments involving CN and ^{13}CN data (see Henkel et al. 1998). While the LVG model result is shown to be inconclusive in Sect. 6.3.2, the CN data suggest that the $[^{12}\text{CO}]/[^{13}\text{CO}]$ ratio is larger than that observed in the galactic center region. Likely explanations are radial infall of ^{13}CO deficient gas from the outer parts of the galaxy or a ^{12}C excess in the ejecta from massive stars (e.g. Henkel & Mauersberger 1993). In agreement with Güsten et al. (1993) we also find that excitation in the south-western and north-eastern lobe is similar. Since our new data allow us to constrain kinetic temperatures to the high end of those predicted by the one component scenario of Güsten et al. ($T_{kin} \gtrsim 30-70 \text{ K}$), our densities are at the low end ($n(\text{H}_2) \lesssim 10^4 \text{ cm}^{-3}$, since the product $T_{kin} n(\text{H}_2)^{1/2}$ is approximately conserved among models simulating optically thick subthermal CO emission). There is a remarkable agreement with respect

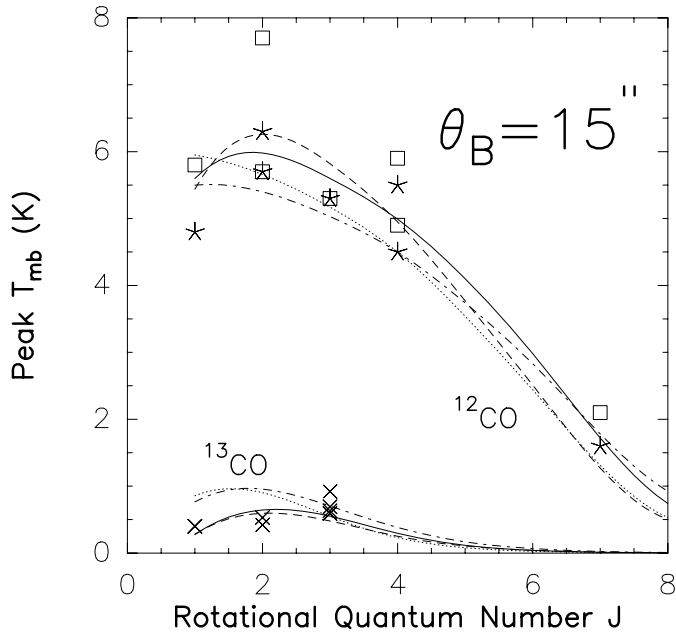


Fig. 7. Peak line temperatures as a function of rotational quantum number J ($J \rightarrow J - 1$) for a beam size of $15''$ toward the south-western (squares) and north-eastern (stars) lobe of M 82. All temperatures were rescaled for coupling the $15''$ beam to a source solid angle (at a given velocity) of $\Omega = 100 \text{ arcsec}^2$ (e.g. Lord et al. 1996). ^{12}CO $J = 1-0$: Nakai et al. (1987; $16''$), this paper ($22''$); $J = 2-1$: Wild et al. (1992; $13''$), this paper ($13''$); $J = 3-2$: Tilanus et al. (1991; $14''$); $J = 4-3$: Güsten et al. (1993; $15''$), this paper ($18''$); $J = 7-6$: this paper ($13''$). ^{13}CO (crosses): $J = 1-0$ and $2-1$: this paper ($22''$ and $13''$); $J = 3-2$: Tilanus et al. (1991; $14''$), this paper ($22''$). Results from radiative transfer calculations are also given (for the parameters, see Fig. 5).

to CO column density, H_2 density, and molecular gas mass between various studies (cf. Tilanus et al. 1991; Wild et al. 1992; Güsten et al. 1993).

6.2. Intrinsic inconsistencies of the model

Our CO data could be reproduced by assuming the presence of two gas components. Selecting such a ‘best’ model, we could discriminate between previously proposed scenarios and could constrain cloud conditions giving rise to highly excited CO emission to slightly higher temperatures and smaller densities than previously suggested. On a deeper level, however, there remain problems. While calculated CO column densities (Sect. 5.1) appear to be correct (see e.g. Fig. 2 of Lo et al. 1987 and Fig. 3 of Smith et al. 1991), an obvious puzzle is the large volume filling factor ($f_{v,22''} \sim 0.05$) that is comparable to the area filling factor (Sect. 5.1). This forced us to postulate a characteristic cloud radius ($r_{\text{cloud}} \sim 150 \text{ pc}$) that encompasses a large part of the studied volume. Such a large cloud radius is inconsistent with the expectation of similar scale lengths along the three dimensions ($f_{v,22''} \sim f_{a,22''}^{3/2}$) and with the *spatial fine structure* deduced from CO (e.g. Shen & Lo 1995; Neininger et al. 1998), high density tracers like HCN and HCO^+ (e.g. Brouillet & Schilke 1993; Paglione et al. 1997; Seaquist et al.

1998), and infrared fine structure lines (e.g. Lugten et al. 1986; Lord et al. 1996).

Another problem is the *density of the gas* observed. A density of $n(\text{H}_2) \lesssim 10^4 \text{ cm}^{-3}$ is small when compared to the prototypical ‘hot core’ associated with the Orion nebula, violating a sometimes noted similarity between these tiny, highly obscured galactic star forming regions and the more extended starbursts studied in external galaxies (e.g. Lo et al. 1987; Wolfire et al. 1990). More seriously, the molecular density determined by us for the starburst in M 82 is smaller than most theoretical studies and observational data permit: Assuming ‘reasonable’ density structure ($n(\text{H}_2) \propto r^{-1 \dots -2}$) and accounting for the intense UV field, Brouillet & Schilke (1993) find that molecular clouds with densities less than a few times 10^4 cm^{-3} should not exist in the central region of M 82. For the transition region between the atomic and molecular gas they propose a density of 10^{4-5} cm^{-3} which disagrees with the range of densities deduced from our LVG analysis in Sect. 5.1 (for cloud stability against tidal stress, see Appendix B).

Studies of high density tracers (e.g. CS, HCN, and HCO^+) commonly reveal densities $n(\text{H}_2) \gtrsim 10^4 \text{ cm}^{-3}$ (e.g. Mauersberger & Henkel 1989; Brouillet & Schilke 1993; Paglione et al. 1997; Seaquist et al. 1998), even for the low excitation component (compare Mauersberger & Henkel 1989 with Baan et al. 1990). In view of $T_{\text{dust}} = 48 \text{ K}$ (Hughes et al. 1994; Colbert et al. 1999), radiative excitation by infrared photons should not significantly alter the density estimates (see Carrol & Goldsmith 1981 and Appendix C). Millimeter wave recombination lines indicate the presence of an ionized component with low filling factor and high electron density ($n_e > 10^{4.5} \text{ cm}^{-3}$; Seaquist et al. 1996). This gas may be associated with a population of (ultra)compact HII regions or with shock ionized dense molecular material. Far infrared fine-structure lines, if tracing the interface between the molecular and the ionized gas, indicate densities of $10^{3.3-4.0} \text{ cm}^{-3}$ (e.g. Lugten et al. 1986; Wolfire et al. 1990; Lord et al. 1996; Stutzki et al. 1997; Colbert et al. 1999) that may agree too well with those derived by us for CO (Sect. 5.1).

An interesting aspect is also provided by *kinetic temperature* estimates: With $T_{\text{kin}} \sim 20-60 \text{ K}$ (Seaquist et al. 1998; this temperature is consistent with the estimated cosmic ray flux; see Völk et al. 1989, Suchkov et al. 1993, and Fig. 2 of Farquhar et al. 1994) the temperature of the dense molecular gas appears to agree fairly well with that of the dust ($T_{\text{dust}} = 48 \text{ K}$; Hughes et al. 1994; Colbert 1999). This is further supported by an apparent lack of CH_3OH and SiO emission, two tracers of high temperature gas that are easily seen in other nearby starburst galaxies (Henkel et al. 1991; Mauersberger & Henkel 1993). The surrounding neutral and ionized layers have larger temperatures, at the order of $50-100$ to 200 K (e.g. Lugten et al. 1986; Wolfire et al. 1990; Lord et al. 1996; Colbert et al. 1999). An analysis of [C I] 492 and 809 GHz emission from the south-western lobe of M 82 (Stutzki et al. 1997) shows a particularly striking similarity in density, temperature, and area (but not volume) filling factor with our LVG parameters derived for CO (Sect. 5.1; the [C I]/CO abundance ratio then becomes ~ 0.4). It seems as if CO were an integral part of the dense atomic gas layers of M 82.

6.3. A PDR model for the CO emission from M 82

6.3.1. General aspects

To resolve inconsistencies related to CO fine scale structure, H₂ density, and kinetic temperature (Sect. 6.2), we note that a significant fraction of the molecular gas in the Milky Way lies in photon dominated regions (PDRs; see Hollenbach & Tielens 1997). A PDR model is also successfully applied to simultaneously explain CO and [CII] line intensities in the central region of the late-type spiral IC 342 that is not a starburst galaxy but that is believed to be a face-on ‘mirror image’ of the galactic center region (Schulz et al. in preparation).

In the central region of M 82 with its high UV flux, the bulk of the interstellar line radiation likely arises from PDRs. As we have seen (Sect. 6.2), the coolest gas component is observed toward the dense cloud cores, a situation that is consistent with the inside-out temperature gradient expected in the case of PDRs. While CO excitation by infrared radiation from the dust can be neglected (see Appendix C), the impact of UV photons may strongly affect rotational level populations and measured CO line intensities in regions with high UV flux. Estimating the far-UV flux (6.0 – 13.6 eV) in the starburst region, Wolfire et al. (1990), Stacey et al. (1991), Lord et al. (1996), and Colbert et al. (1999) find $\chi \sim 10^{2.8-3.9}$ (χ : incident far-UV flux in units of the local galactic flux, $1.6 \cdot 10^{-3} \text{ erg s}^{-1} \text{ cm}^{-2}$). Such a high value leads to outer cloud layers that are predominantly heated by collisions with electrons photoejected from dust grains or through collisional deexcitation of vibrationally excited, UV-pumped H₂.

Exploring effects of finite cloud size for clumps with plane-parallel geometry, Köster et al. (1994) presented comprehensive computations of CO rotational line intensities from PDRs. In contrast to the constant temperature LVG treatment presented in Sect. 5, PDR models account for strong kinetic temperature gradients. The low- J lines typically arise from deeper inside the clouds than the mid- J lines observed by us (Sect. 3.1). Reproducing observed line ratios of optically thick ¹²CO emission, PDR model densities are larger than those derived from a one temperature, one density LVG model. PDR line intensity ratios only surpass unity if the higher- J line has a critical density (for the values, see Sect. 1) that is smaller than the actual gas density. Then, both lines are approximately thermalized but the higher J -line is emitted from warmer layers further out. For densities at the order of $5 \cdot 10^3 \text{ cm}^{-3}$ (the density deduced from our one component LVG model in Sect. 5.1), ¹²CO PDR line temperatures rapidly decrease with rotational quantum number J . For $\chi \sim 10^3$ and $N(\text{H}_2) \sim 10^{22} \text{ cm}^{-2}/\text{km s}^{-1}$ (Sect. 5.1), densities are then at the order of 10^4 and 10^5 cm^{-3} for the low and high excitation components, respectively.

For the gas with *low CO excitation*, a density of $n(\text{H}_2) \sim 10^4 \text{ cm}^{-3}$ is sufficiently high to explain the detection of CS $J = 2-1$ emission (e.g. Mauersberger & Henkel 1989; Baan et al. 1990). A density of $n(\text{H}_2) \sim 10^5 \text{ cm}^{-3}$ in the *high excitation* region would fulfill all theoretical (Brouillet & Schilke 1993) and observational density requirements outlined in Sect. 6.2. Furthermore, the volume filling factor $f_{v,22''} = \langle n(\text{H}_2) \rangle_{22''}/n(\text{H}_2)$

would drop by one to two orders of magnitude below the value estimated in Sect. 5.1. If the area filling factor is not drastically altered, this yields reasonable molecular cloud radii $\lesssim 10 \text{ pc}$ (see Sect. 5.1 and Lugten et al. 1986; Wolfire et al. 1990; Brouillet & Schilke 1993; Shen & Lo 1995; Seaquist et al. 1996; Stutzki et al. 1997). The apparently intermediate temperature of the CO emitting gas between those of the dust and the dense atomic medium is naturally explained by mid- J CO emission predominantly arising in the heated surface layers of dense molecular clouds.

To summarize: PDR simulations of ¹²CO emission remove inconsistencies related to spatial fine scale structure, density, and kinetic temperature. So far published PDR results fail however when ¹³CO is also considered. Calculated ¹²CO/¹³CO line intensity ratios are much smaller than the ratios observed (see Table 1 and Köster et al. 1994) and a more detailed numerical analysis is therefore needed.

6.3.2. PDR model calculations

For a numerical approach we note that the beam averaged column density ($N(\text{H}_2)_{22''} \sim 10^{23} \text{ cm}^{-2}$) and the beam averaged density ($\langle n(\text{H}_2) \rangle_{22''} \sim 200 \text{ cm}^{-3}$) are observationally determined (Sects. 5.1 and 6.2) and do not depend on the choice of the excitation model if a significant fraction of the dust is associated with molecular clouds. Complementing these boundary conditions, we obtain (cf. Sect. 5.1)

$$\frac{r_{\text{cloud}}}{[\text{pc}]} \sim 175 \frac{200 \text{ cm}^{-3}/n(\text{H}_2)_{\text{PDR}}}{T_{\text{CO,observed}}/T_{\text{CO,PDR}}} \quad (1)$$

and

$$\frac{N(\text{H}_2)_{\text{PDR}}}{[\text{cm}^{-2} \text{ km s}^{-1}]} \sim \frac{10^{23}/300}{T_{\text{CO,observed}}/T_{\text{CO,PDR}}} \quad (2)$$

with $200 \text{ cm}^{-3}/n(\text{H}_2)_{\text{PDR}}$ denoting the volume filling factor, $T_{\text{CO,observed}}/T_{\text{CO,PDR}}$ being the area filling factor, $n(\text{H}_2)_{\text{PDR}}$ giving the average density, and $N(\text{H}_2)_{\text{PDR}}$ representing the average column density of an individual clump per km s^{-1} (300 km s^{-1} is the total CO linewidth of the nuclear region of M 82; $N(\text{H}_2)_{\text{PDR}} = (4/3) \cdot r_{\text{cloud}} \cdot n(\text{H}_2)_{\text{PDR}}$ and $n(\text{H}_2)_{\text{PDR-cloud-surface}} = 0.5 \cdot n(\text{H}_2)_{\text{PDR}}$ for the assumed cloud geometry and density structure, see below).

Since embedded clumps of dense gas may more often be spherical than plane-parallel, spherical clouds with a power law density distribution ($n(r) \sim r^{-1.5}$) were modeled with the dust being heated by the external UV radiation and intrinsic infrared emission (cf. Störzer et al. 1996; 2000). While we can reproduce the observed relative intensities of the various rotational CO transitions with a density at the order of $n(\text{H}_2) \sim 10^5 \text{ cm}^{-3}$ (see Fig. 8 and Sect. 6.3.1), r_{cloud} and $N(\text{H}_2)$ are inconsistent with Eqs. 1 and 2. Furthermore, computed ¹²CO/¹³CO line intensity ratios show little dependence on cloud structure and remain with characteristic values of 2–4 (see also Gierens et al. 1992 for ¹²C/¹³C = 40; Köster et al. 1994 and Störzer et al. 2000 for ¹²C/¹³C = 67) much smaller than the observed ratios of 10–15 (see Table 1). Varying χ over the permitted range ($10^{3.3 \pm 0.4}$)

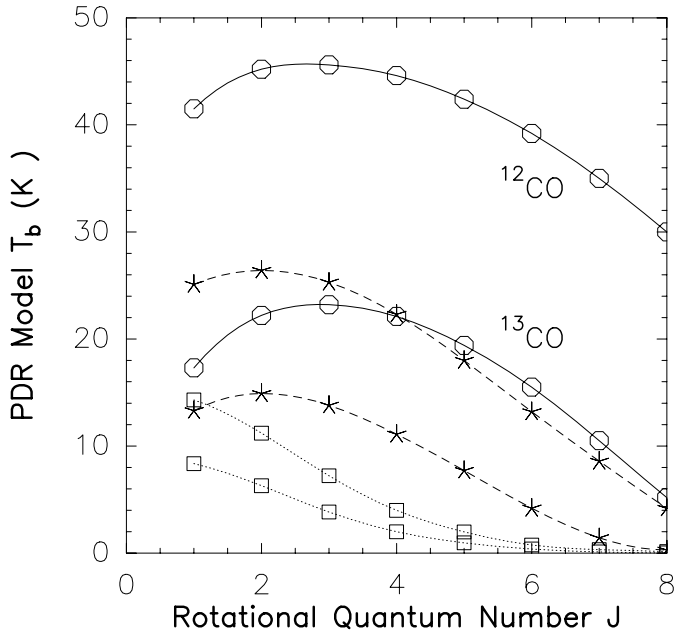


Fig. 8. PDR model peak line temperatures as a function of rotational quantum number J ($J \rightarrow J-1$) for clouds with high column density. Dotted lines with open squares: $n(\text{H}_2) = 2 \cdot 10^4 \text{ cm}^{-3}$, the curve with high T_b displays ^{12}CO , the lower one ^{13}CO ; dashed lines with asterisks: $n(\text{H}_2) = 2 \cdot 10^5 \text{ cm}^{-3}$; solid lines with open circles: $n(\text{H}_2) = 2 \cdot 10^6 \text{ cm}^{-3}$. For all models, $N(\text{H}_2) = 2 \cdot 10^{22} \text{ cm}^{-2}$, implying cloud radii of $7.5 \cdot 10^{17}$, $7.5 \cdot 10^{16}$, and $7.5 \cdot 10^{15} \text{ cm}$, respectively. Assumed linewidth of an individual cloud and its carbon isotope ratio: 1.2 km s^{-1} and 67. For the definition of $n(\text{H}_2) = n(\text{H}_2)_{\text{PDR}}$, see Sect. 6.3.2.

does not change these line intensity ratios significantly. Drastically increasing the carbon isotope ratio leads to $^{12}\text{C}/^{13}\text{C} > 100$ which is inconsistent with data from the solar system, the Milky Way, and the Magellanic Clouds (e.g. Wilson & Rood 1994; Chin et al. 1999).

Other parameters that can be varied are the density and column density of the far-UV irradiated cloud. The ^{12}CO lines are formed in warm layers near the surface whereas ^{13}CO lines are predominantly emitted from cooler regions deeper inside. With the column density being fixed, a higher density leads to a moderate increase in the $^{12}\text{CO}/^{13}\text{CO}$ line intensity ratio (see Fig. 8), because ^{12}CO is then emitted from CO layers closer to the heated cloud surface. To reproduce observed $^{12}\text{CO}/^{13}\text{CO}$ line ratios in this way requires, however, densities $\gtrsim 10^8 \text{ cm}^{-3}$.

More important are variations in column density: A spherical UV illuminated cloud is effectively smaller in ^{13}CO than in ^{12}CO and this difference becomes more pronounced when $N(\text{H}_2)$ decreases (see Störzer et al. 2000). In the extreme case of totally photodissociated ^{13}CO , some ^{12}CO may still exist in the clump so that, in principle, $^{12}\text{CO}/^{13}\text{CO}$ line intensity ratios up to very large values can be reproduced. Once the ^{13}CO abundance gets very small, ^{12}CO also tends to become optically thin. In Fig. 9 we show expected line temperatures in this optically thin regime, with $n(\text{H}_2) = 5 \cdot 10^3 \text{ cm}^{-3}$ successfully reproducing measured ^{12}CO line intensity ratios for the *high CO excitation component*. $^{12}\text{CO}/^{13}\text{CO} = 19, 10, 8.5, 9.4, 13, 20,$ and 30 for $J =$

Table 4. PDR model parameters

		Footnote
<i>High excitation comp.</i>		
$^{12}\text{CO}/^{13}\text{CO}$	undetermined	a
$n(\text{H}_2)$	$\sim 10^{3.7} \text{ cm}^{-3}$	
$f_{a,22''}$	$\sim 15-200$	b
$f_{v,22''}$	~ 0.05	c
$N(\text{CO})_{22''}$	$\sim 5 \cdot 10^{18} \text{ cm}^{-2}$	d
$N(\text{H}_2)_{22''}$	$\sim 10^{23} \text{ cm}^{-2}$	d
$N(\text{H}_2)_{\text{cloud}}$	$\sim 5 \cdot 10^{20} \text{ cm}^{-2}/\text{km s}^{-1}$	e
$\langle n(\text{H}_2) \rangle_{22''}$	$\sim 200 \text{ cm}^{-3}$	
r_{cloud}	$\sim 0.025 \text{ pc}$	f
$M_{\text{mol},22''}$	$\sim 1-7 \cdot 10^8 M_{\odot}$	
<i>Low excitation comp.</i>		
$n(\text{H}_2)$	$\sim 10^3 \text{ cm}^{-3}$	
$f_{a,22''}$	~ 15	b
r_{cloud}	$\sim 0.15 \text{ pc}$	f

a $^{12}\text{CO}/^{13}\text{CO}$: abundance ratio

b $f_{a,22''}$: Area filling factor for the central $22''$; the lower value is derived from a comparison of modelled and observed line intensities, the higher value results from a comparison of total $22''$ beam averaged and individual cloud column density.

c $f_{v,22''}$: Volume filling factor for the central $22''$ (see Sect. 5.1)

d $N(\text{CO})_{22''}$, $N(\text{H}_2)_{22''}$: $22''$ beam averaged total column density

e $N(\text{H}_2)_{\text{cloud}}$: Column density of an individual cloud

f r_{cloud} : Characteristic molecular cloud size

1–0... 7–6, respectively. This is compatible with observed ratios of 15, 10, and 9 for the three lowest rotational transitions. For the *low excitation component*, $n(\text{H}_2) \sim 10^3 \text{ cm}^{-3}$; Fig. 9 shows a fit with $^{12}\text{CO}/^{13}\text{CO} = 17, 10,$ and 11 for $J = 1-0$ to $3-2$.

It is remarkable that *PDR model densities are similar to those derived with our LVG simulation*, contradicting theoretical predictions of minimum densities in excess of 10^4 cm^{-3} (Brouillet & Schilke 1993). *Column densities* ($N(\text{H}_2) \sim 5 \cdot 10^{20} \text{ cm}^{-2}/\text{km s}^{-1}$) and *line temperatures of individual cloudlets* are, however, drastically different. An average cloudlet shows optically thin, not optically thick CO line emission. Line temperatures of individual clumps are much smaller than the observed average over the inner 300 pc, so that the *PDR area filling factor* f_a is not $\ll 1$ as in the LVG approximation but $\gg 1$. Thus not a higher density (as anticipated in Sect. 6.3.1) but a higher f_a leads to plausible r_{cloud} values in the sub-parsec range (see Eq. 1). Both $f_a \gg 1$ and $r_{\text{cloud}} < 1 \text{ pc}$ are consistent with early CO studies, favoring CO lines of low optical depth. These conclusions are supported by observations of fine-structure lines in the infrared (e.g. Olofsson & Rydbeck 1984; Lugten et al. 1986; Wolfire et al. 1990; Brouillet & Schilke 1993; Schilke et al. 1993; Lord et al. 1996). In view of our PDR simulations, the high density ($> 10^{4.5} \text{ cm}^{-3}$) ionized gas found by Seaquist et al. (1996) is likely related to (ultra)compact HII regions and not to evaporating dense molecular clouds.

Obviously, our study does not imply that the core of M 82 does not contain regions of high density and column density. The *bulk of the CO emission*, however, *must arise from a warm*

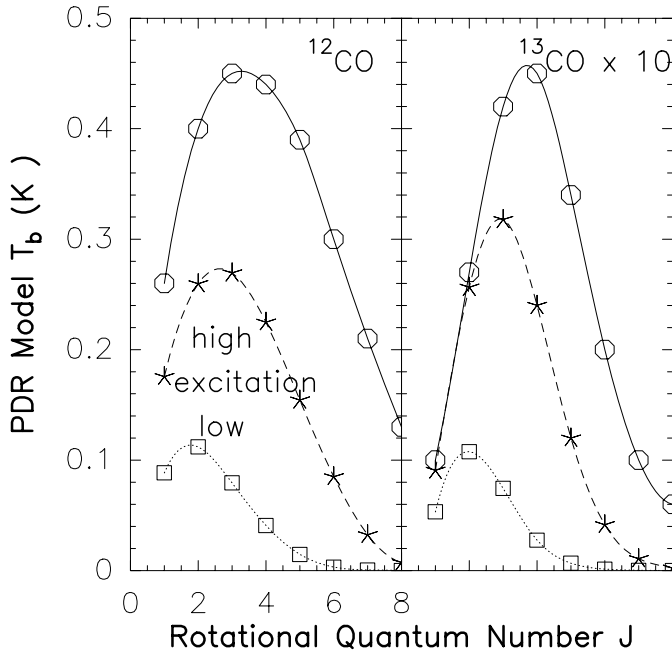


Fig. 9. PDR model peak line temperatures as a function of rotational quantum number J ($J \rightarrow J - 1$) for low column density clouds, reproducing line intensity ratios for the ‘high’ and ‘low’ CO excitation components. Dotted lines with open squares (‘low excitation’): $n(\text{H}_2) = 10^3 \text{ cm}^{-3}$, $r_{\text{cloud}} = 4.5 \cdot 10^{17} \text{ cm}$, and $N(\text{H}_2) = 6 \cdot 10^{20} \text{ cm}^{-2}$; dashed lines with asterisks (‘high excitation’): $n(\text{H}_2) = 5 \cdot 10^3 \text{ cm}^{-3}$, $r_{\text{cloud}} = 7.5 \cdot 10^{16} \text{ cm}$, and $N(\text{H}_2) = 5 \cdot 10^{20} \text{ cm}^{-2}$; solid lines with open circles: $n(\text{H}_2) = 2 \cdot 10^4 \text{ cm}^{-3}$, $r_{\text{cloud}} = 1.5 \cdot 10^{16} \text{ cm}$, and $N(\text{H}_2) = 4 \cdot 10^{20} \text{ cm}^{-2}$. Assumed linewidth of an individual cloud and its carbon isotope ratio: 1.2 km s^{-1} and 67, respectively. For the definition of $n(\text{H}_2) = n(\text{H}_2)_{\text{PDR}}$, see Sect. 6.3.2.

low density interclump medium. The gas may be barely dense enough to avoid tidal disruption (see Appendix B). For typical cloud cores in the galactic disk, Eq. 5 of Larson (1981) predicts a column density of $N(\text{H}_2) \sim 10^{22} \text{ cm}^{-2}$. With $N(\text{H}_2) \sim 5 \cdot 10^{20} \text{ cm}^{-2}/\text{km s}^{-1}$ (Table 4) this infers a linewidth of 20 km s^{-1} . The relations defined for approximately virialized clouds by Larson (1981) then yield cloud sizes well in excess of 100 pc, in strong contradiction with our PDR model. *The bulk of the CO emission therefore arises from gas that may not be virialized. We conclude that CO is tracing a different gas component than molecular high density tracers like CS or HCN. The dominance of CO emission from a diffuse medium with cloud fragments of low column density per km s^{-1} , $X = N(\text{H}_2)/I_{\text{CO}}$ conversion ratio, and CO intensity explains why HCN is a better tracer of star formation and infrared luminosity (Solomon et al. 1992a). It also explains why $[\text{C}1]/\text{CO}$ abundance ratios are higher than those observed in spatially confined star forming regions of the galactic disk (see also Sect. 6.2, Schilke et al. 1993, and White et al. 1994).*

An argument against our scenario could be that Eqs. 1 and 2 only hold approximately: The denominator $T_{\text{CO,observed}}/T_{\text{CO,PDR}}$ is too small by an order of magnitude to yield the proper r_{cloud} value assumed in the PDR approxi-

mation, while it is too large by the same amount to provide the proper $N(\text{H}_2)_{\text{PDR}}$ value. In order to check whether our scenario is plausible, we therefore extend our analysis to other galaxies.

6.4. Other galaxies

6.4.1. The Milky Way and other ‘quiescent’ galaxies

Studying the physics of the molecular gas in the galactic center region, Dahmen et al. (1998) compared ^{12}CO and $\text{C}^{18}\text{O } J=1-0$ data obtained with a linear resolution of $\sim 22 \text{ pc}$ ($8'$). Lineshapes, spatial distributions, and line ratios indicate the presence of an extended diffuse gas component that is not apparent in studies focusing on individual cloud cores (see also Oka et al. 1998a). A significant fraction of the gas is not virialized. Higher resolution data (e.g. Hüttemeister et al. 1998) reveal that the dense molecular gas ($n(\text{H}_2) \gtrsim 10^4 \text{ cm}^{-3}$) is relatively cool ($T_{\text{kin}} \sim 25 \text{ K}$) in comparison to that at lower density ($\sim 100 \text{ K}$ at a few 10^3 cm^{-3}). Apparently, a warm diffuse molecular medium is not only ubiquitous in the starburst galaxy M 82 but also dominates the CO emission in the more quiescent central region of the Milky Way (for extended CO maps of a galactic disk star forming region, see Wilson et al. 1999). This also holds for the nuclear regions of IC 342 (Schulz et al. in preparation) and NGC 7331 (Israel & Baas 1999), another two galaxies with $L_{\text{FIR}} \sim 10^{10} L_{\odot}$. Like M 82, NGC 7331 shows a warmer inner and cooler outer dust ring and a molecular ring that appears to be related to its cool dust component.

Shocks and cloud-cloud collisions induced by the presence of bars (e.g. Achtermann & Lacey 1995; Morris & Serabyn 1996; Fux 1997, 1999; Hüttemeister et al. 1998), tidal disruption of clouds near the center (Güsten 1989), a high gas pressure (e.g. Helfer & Blitz 1997) that can help to keep the gas molecular, and a high stellar density that can affect molecular cloud dynamics (e.g. Mauersberger et al. 1996b; Oka et al. 1998b) may all contribute to the disintegration of molecular clouds and to the synthesis of an extended warm molecular spray consisting of low column density cloud fragments.

6.4.2. Nearby starburst galaxies

So far, M 82 is the only starburst galaxy where we could show that a CO-LVG excitation analysis (inferring $f_v \sim f_a$; see Sect. 5.1) does not lead to results that are free of inconsistencies. The lack of CO $J=7-6$ data does not constrain LVG parameters sufficiently to search for a similar discrepancy in the other two nearby starburst galaxies NGC 253 and NGC 4945. This implies that previous studies did not provide sufficient motivation to replace LVG excitation analyses by PDR scenarios.

Towards NGC 253, M 82, and NGC 4945 ^{12}CO and $^{12}\text{CO}/^{13}\text{CO}$ line intensity ratios are similar. This even holds for absolute integrated line intensities (within 30%) for a $22-24''$ beam size (compare Table 1 with Mauersberger et al. 1996a,b; Harrison et al. 1999). Not surprisingly, published LVG densities and area filling factors for NGC 253 and NGC 4945 match those for M 82 (Henkel et al. 1994; Mauersberger et al.

1996a,b; Harrison et al. 1999). Following the procedure outlined in Sect. 5.1, average densities along the line-of-sight ($\langle n(\text{H}_2) \rangle \sim 100 \text{ cm}^{-3}$) yield volume filling factors at the order of $f_{v,22''} = \langle n(\text{H}_2) \rangle / n(\text{H}_2) \sim 0.02$. Since volume filling factors seem to be slightly smaller than area filling factors, average cloud sizes become $\sim 30 \text{ pc}$ (for the Milky Way, see Oka et al. 1998b), not enough to request the use of PDR models.

Because of the similarity of CO line strengths and line ratios and since high [C I]/CO ratios are observed toward both M 82 and NGC 253 (Schilke et al. 1993; White et al. 1994; Harrison et al. 1995; Israel et al. 1995; Stutzki et al. 1997) we nevertheless feel that PDR simulations relating the bulk of the CO emission to a warm diffuse molecular medium are relevant not only to M 82 but to NGC 253 and NGC 4945 as well.

6.4.3. Mergers

Active disk galaxies exhibit $^{12}\text{CO}/^{13}\text{CO}$ ratios ~ 10 (this is independent of inclination, Hubble Type, and metallicity; Sage & Isbell 1991). Perturbed gas-rich mergers with infrared luminosities $\gtrsim 10^{11} L_{\odot}$ tend to show larger values, up to 40–60 (Henkel & Mauersberger 1993). This may be caused by excitation effects (see Aalto et al. 1999) or by a deficiency of ^{13}CO emission since L_{FIR} is better correlated with ^{12}CO (Taniguchi & Ohya 1998). Inflow of gas from the outer disks may provide ^{13}CO deficient gas and nucleosynthesis in shortlived massive stars may further enhance ^{12}C (Casoli et al. 1992). While this may help to enhance $^{12}\text{CO}/^{13}\text{CO}$ line intensity ratios, this is not sufficient to explain measured $^{12}\text{CO}/^{13}\text{CO}$ values within the context of PDRs. Instead we suggest that the direct interaction of two galactic nuclei and their associated disks is even more efficient than the presence of a bar to trigger cloud-cloud collisions and to create a warm diffuse molecular debris containing a large number of small cloud fragments. If such fragments are smaller than in individual non-merging galaxies, higher $^{12}\text{CO}/^{13}\text{CO}$ line ratios might result. While the detailed spatial CO fine-structure may only be revealed by next generation mm-wave telescopes (e.g. Downes 1999), this would imply that in mergers with $^{12}\text{CO}/^{13}\text{CO} \gg 10$, [C I]/CO line intensity ratios should be as large as or *even larger* than in M 82 and NGC 253. For a first detection of [C I] in a merger, see Gerin & Philips (1998).

6.4.4. Galaxies at high redshifts

Is it a general property of the integrated spectrum of a starburst that, beginning with the CO $J = 4-3$ transition, line intensities (accounting for beam dilution) gradually decrease with increasing rotational quantum number J ? Ground based measurements of nearby galaxies in mid and high- J CO transitions require exceptional weather conditions. In galaxies of high redshift, however, many otherwise inaccessible transitions are shifted into the observable mm- and submm-wavelength bands. While linear resolutions remain poor, the bulk of the CO emission from higher excited states should arise from the nuclear starburst environment. Suitable examples of distant sources with

a number of detected CO transitions are IRAS F 1024+4724 ($z = 2.286$), the Cloverleaf quasar ($z = 2.558$), and BR 1202–0725 ($z = 4.692$). Toward IRAS F 1024+4724, the $J = 3-2$ line is stronger than the 4–3 and 6–5 lines; line intensity ratios w.r.t. 3–2 are ~ 0.75 and 0.6 (Solomon et al. 1992b). Toward the Cloverleaf quasar, CO lines are characterized by a constant or increasing brightness temperature from 3–2 to 4–3, followed by constant or (more likely) decreasing line intensities in the higher J transitions (Barvainis et al. 1997). Toward BR 1202–0725, the $J = 7-6$ to 5–4 line intensity ratio is ~ 0.65 (Omont et al. 1996). Although the sample is too small for a reliable statistical analysis, it seems that CO line intensity ratios are fairly uniform in starbursts and depend little on redshift (age) and temperature ($T_{\text{cmb}}/[\text{K}] = 2.73(1+z)$) of the microwave background. Unfortunately, $^{12}\text{CO}/^{13}\text{CO}$ line intensity ratios are not yet known. If they are $\gtrsim 10$, densities at the order of a few 10^3 cm^{-3} and small column densities ($\lesssim 10^{21} \text{ cm}^{-2}/\text{km s}^{-1}$) should be a characteristic feature for the bulk of the CO emitting cloudlets in all starburst galaxies.

7. Conclusions

We have studied millimeter and submillimeter CO line emission up to the $J = 7-6$ rotational transition toward the central region of the starburst galaxy M 82 and obtain the following main results:

- (1) The spatial structure of the millimeter and submillimeter CO emission is distinct. While integrated intensity maps suggest that the lobe separation of the low- J transitions is $\sim 26''$, it is $\sim 15''$ for the mid- J transitions. Major-axis position-velocity maps in the CO $J = 2-1$ and 4–3 lines show however agreement in the lobe positions. This indicates that, at the inner edges of the low- J CO lobes, line profiles are wider in the higher excited CO transitions. We thus distinguish between a ‘low’ and a ‘high’ CO excitation component, the latter coinciding with the main source of millimeter and submillimeter dust emission.
- (2) An LVG excitation analysis of CO submillimeter lines leads to internal inconsistencies. While measured line intensities are reproduced with $T_{\text{kin}} \sim 60 - 130 \text{ K}$, $n(\text{H}_2) \sim 10^{3.3-3.9} \text{ cm}^{-3}$, cloud averaged column densities $N(\text{CO})_{\text{cloud}} \sim 10^{20}$ and $N(\text{H}_2)_{\text{cloud}} \sim 10^{24-25} \text{ cm}^{-2}$, $[^{12}\text{CO}]/[^{13}\text{CO}]$ abundance ratios $\gtrsim 50$, and a total molecular mass of a few $10^8 M_{\odot}$, area filling factors ($f_a \sim 0.05-0.10$) and volume filling factors ($f_v \sim 0.05$) are similar. This results in cloud sizes that do not match their angular scale. On the other hand, the resulting H_2 column density is consistent with that derived from the dust continuum at millimeter and submillimeter wavelengths. For the low excitation component, densities are $\sim 10^3 \text{ cm}^{-3}$.
- (3) An application of PDR models resolves the inconsistencies of the LVG calculations. LVG densities, column densities, and total mass are confirmed. The bulk of the CO emission arises, however, from a diffuse, low column density ($N(\text{H}_2) \sim 5 \cdot 10^{20} \text{ cm}^{-2}/\text{km s}^{-1}$) interclump medium with

small $X = N(\text{H}_2)/I_{\text{CO}}$ conversion factors, area filling factors $\gg 1$, and sub-parsec cloud sizes. The relations defined by Larson (1981) are not fulfilled and the gas may not be virialized. Such a scenario explains why CS or HCN are better tracers of global star formation rate and infrared luminosity than CO. Our scenario also explains observed high [C I]/CO line intensity ratios, while relative abundances of ^{12}CO versus ^{13}CO cannot be accurately determined. Higher column density clouds, even accounting for variations in far-UV flux and $^{12}\text{C}/^{13}\text{C}$ isotope ratios, do not reproduce observed $^{12}\text{CO}/^{13}\text{CO}$ line intensity ratios $\gtrsim 10$. Densities are close to the minimum values required for tidal stability in the absence of magnetic fields.

- (4) In regard to ^{12}CO line intensity ratios, the central region of M 82 appears to be representative for the entire family of starburst galaxies, both at small and at high redshifts. A comparison of the starburst regions in M 82 and NGC 253 demonstrates that this similarity extends to $^{12}\text{CO}/^{13}\text{CO}$ and [C I]/CO line intensity ratios. The large $^{12}\text{CO}/^{13}\text{CO}$ line intensity ratios ($\gg 10$) observed toward ‘nearby’ mergers prove, however, that differences exist at least w.r.t. rare CO isotopomers. Galaxy pairs with such high $^{12}\text{CO}/^{13}\text{CO}$ line intensity ratios require the presence of a particularly diffuse highly fragmented low column density ISM.

Apparently, dropping the assumption of constant temperature in the CO excitation model is a necessary step to provide a self-consistent approach to the physical properties of molecular clouds in the nuclear starburst region of M 82. While the use of PDR models is crucial for a better understanding of the molecular gas phase in a starburst environment, important information is still missing. Interferometric observations of high density tracers (e.g. CN, CS, HCN, HNC, N_2H^+), coupled with PDR model calculations including chemical aspects, are needed to fully understand the spatial morphology, density distribution, and molecular excitation of this archetypical starburst complex. An interesting aspect is provided by HCO^+ $J = 1-0$ line emission (Table 2). The bulk of this emission might arise from regions intermediate between those of the low and high CO excitation component. Since this molecule (as well as N_2H^+) is a sensitive tracer of ionization conditions in the dense gas, a detailed knowledge of its spatial distribution would be crucial for a better understanding of structure and excitation.

So far, models were calculated for the cosmic ray flux of the solar neighbourhood. A flux enhancement by two to three orders of magnitude (with all necessary chemical implications) has still to be incorporated into PDR codes (but see Schilke et al. 1993). Another important quantity is the spatial distribution of the UV flux. For M 82, we do not know the variation of the UV flux as a function of galactocentric radius.

Acknowledgements. It is a pleasure to thank the HHT staff, in particular H. Butner, B. Hayward, D. Muders, F. Patt, and B. Stupak, for their enthusiastic support of the project and for their flexibility in changing schedules according to variable weather conditions. For the permission to use the HEB, we also thank the Harvard-Smithsonian Center for Astrophysics (CfA). We acknowledge useful discussions with S.

Hüttemeister, E. Ros, P. Schilke, C.M. Walmsley, A. Weiß, and the useful comments of an anonymous referee. R.Q.M. acknowledges support by the exchange program between the Chinese Academy of Sciences and the Max-Planck-Gesellschaft; C.H. acknowledges support from NATO grant SA.5-2-05 (CRG. 960086) 318/96.

Appendix A: the radiative transfer model

Systematic motions and microturbulence are frequently used as simplifying assumptions to facilitate treatment of line formation in molecular clouds. For the large amplitude systematic motions assumed in the Large Velocity Gradient (LVG) approximation, the source functions are locally defined. For the homogeneous velocity field assumed in the microturbulent approximation, the source functions are generally coupled throughout the cloud by scattered radiation. The crucial difference between the two approximations is that between local and non-local excitation and both can be viewed as limiting cases for the treatment of molecular line formation. In the case of CO, line intensities determined with a standard LVG model (e.g. Castor 1970; Scoville & Solomon 1974) do not differ by more than a factor of three from models using the microturbulent approach (White 1977; see also Ossenkopf 1997). This is within the uncertainties that can be attributed to cloud geometry. Furthermore, Wild et al. (1992) found no significant difference between results from their ‘clumpy cloud’ and standard LVG models. Given the inhomogeneity of the ISM, the assumption of uniform physical conditions is crude and only yields average gas properties. In view of the limited quality of the available data and the lack of information on source morphology and its fine-scale structure, however, an LVG treatment of the radiative transfer is an appropriate first step to analyse M 82.

Applying our LVG model to simulate a cloud of spherical geometry, CO collisional cross sections were taken from Green & Chapman (1978). For $T_{\text{kin}} > 100$ K, we assumed collision rates $C_{ij} \propto T_{\text{kin}}^{1/2}$. Using instead the collision rates recommended by De Jong et al. (1975; these include higher temperatures) leads to similar results. A comparison of $J=2-1/J=1-0$ line intensity ratios with those of Castets et al. (1990), that were computed with yet another set of collision rates, also shows consistency within 20%.

Fig. A.1 displays our calculated CO 7–6/4–3 and CO 4–3/ ^{13}CO 3–2 line intensity ratios as a function of density (10^{2-7} cm^{-3}), kinetic temperature (5–150 K), $^{12}\text{CO}/^{13}\text{CO}$ abundance ratio (25–75), and CO fractional abundance in terms of $X(\text{CO})/\text{grad } V$ ($10^{-6 \dots -3} \text{ pc/km s}^{-1}$; $X(\text{CO})$ is the fractional abundance parameter, $\text{grad } V$ denotes the velocity gradient in $\text{km s}^{-1}/\text{pc}$). The choice of $X(\text{CO})/\text{grad } V$ is motivated by a source size of ~ 300 pc and a velocity range of $\sim 300 \text{ km s}^{-1}$ (this leads to $\text{grad } V \sim 1 \text{ km s}^{-1} \text{ pc}^{-1}$), a solar system [C]/[H] abundance ratio of $3.5 \cdot 10^{-4}$ (Grevesse et al. 1994), and the assumption that a significant fraction of the available carbon ($\gtrsim 10\%$) is forming CO molecules. Since molecular clouds with significant CO 7–6 emission must be warm, strong CO fractionation in favor of enhanced ^{13}C abundances (cf. Watson et al. 1976) can be excluded. Fig. A.1 thus presents calculations

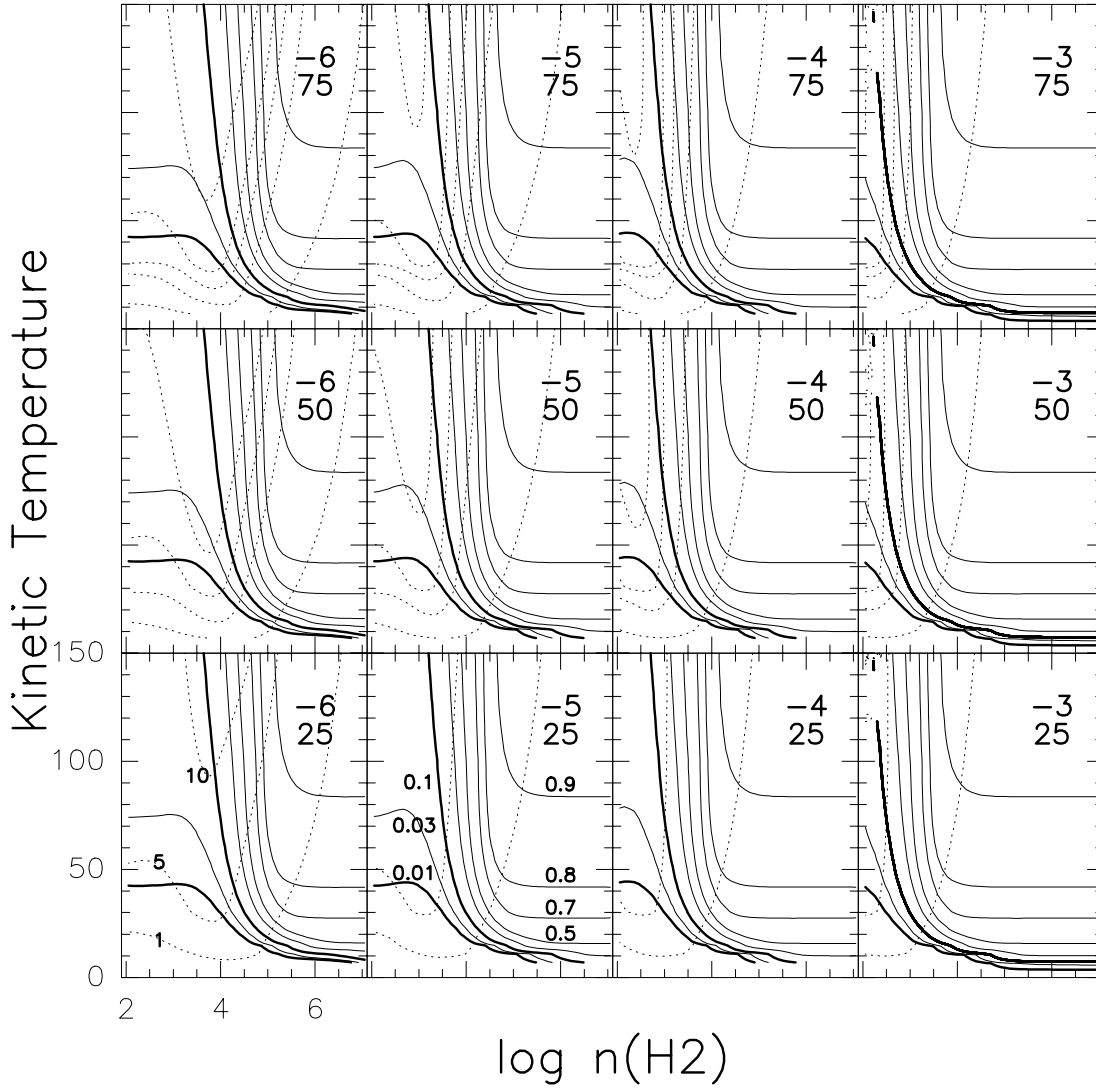


Fig. A.1. Large Velocity Gradient (LVG) model results for $X(\text{CO})/\text{grad } V = 10^{-6}, 10^{-5}, 10^{-4},$ and $10^{-3} \text{ pc/km s}^{-1}$ ($X(\text{CO})$ is the fractional CO abundance parameter) and $^{12}\text{CO}/^{13}\text{CO}$ abundance ratios of 25, 50, and 75. The logarithm of $X(\text{CO})/\text{grad } V$ and the $^{12}\text{CO}/^{13}\text{CO}$ abundance ratio are given for each box in the upper right hand corner. Solid lines: CO 7–6/4–3 line intensity ratios (contour levels from lower left to upper right: 0.01, 0.03, 0.1, 0.3, 0.5, 0.7, 0.8, and 0.9). Dotted lines: ^{12}CO 4–3/ ^{13}CO 3–2 line intensity ratios (contour levels from lower right to upper left: 1., 5., 10., 15., and 25.; for $^{12}\text{CO}/^{13}\text{CO} = 25$, line intensity ratios are <15 , for $^{12}\text{CO}/^{13}\text{CO} = 50$, line intensity ratios are <25).

for $^{12}\text{CO}/^{13}\text{CO} = 25$ (the carbon isotope ratio in the galactic center region; e.g. Wilson & Rood 1994), $^{12}\text{CO}/^{13}\text{CO} = 50$ (the $^{12}\text{C}/^{13}\text{C}$ ratio in the inner galactic disk; e.g. Henkel et al. 1985), and $^{12}\text{CO}/^{13}\text{CO} = 75$ (close to the carbon isotope ratio of the local ISM and the solar system; e.g. Stahl et al. 1989; Stahl & Wilson 1992).

Appendix B: cloud stability

In order for a cloud to be gravitationally bound, it must be sufficiently dense to withstand the tidal stresses caused by the gravitational potential of the galaxy. Neglecting rotation, turbulence, and magnetic fields, and compensating tidal forces by a cloud's own gravity, we can derive a minimum density that is required for survival in a hostile medium. With $V_{\text{rot}} \sim 140 \text{ km s}^{-1}$ at a

galactocentric radius of $R \gtrsim 75 \text{ pc}$ from the dynamical center of M 82 (Neininger et al. 1998) and applying Eq. 5 of Güsten and Downes (1980), we find a limiting cloud density of $n_{\text{min}} \sim 10^{3.2-3.5} [R/120 \text{ pc}]^{-2} \text{ cm}^{-3}$. $R = 120 \text{ pc}$ refers to the molecular lobes of M 82, located at offsets $\pm 7''5$ from the dynamical center of the galaxy (see Table 2). The minimum density n_{min} is near the lower limit of the densities deduced in Sect. 5.1 with an LVG model and just matches densities derived in Sect. 6.3.2 with a PDR model.

Appendix C: radiative pumping

Because the kinetic temperature is constrained by the CO $J=7-6/J=4-3$ line temperature ratios (Table 1), collisional excitation to excited vibrational or electronic levels, $\gtrsim 3000 \text{ K}$ above

the ground state, is not effective. Densities and temperatures obtained with Fig. A.1 might however be affected by radiative excitation, that is neglected in our LVG treatment (apart of the 2.7 K microwave background).

To operate efficiently, radiative pumping must be faster than the collisional rates for rotational excitation in the $v = 0$ vibrational ground state. With $\langle\sigma v\rangle \sim 2 \cdot 10^{-11} \text{ cm}^3 \text{ s}^{-1}$ (Green & Chapman 1978) and a density of $5 \cdot 10^3 \text{ cm}^{-3}$, collision rates are at the order of 10^{-7} s^{-1} . Direct rotational excitation by $\lambda \sim 1 \text{ mm}$ photons from the dust is inefficient, because $\tau_{\text{dust}} \ll 1$. For vibrational excitation by $4.7 \mu\text{m}$ photons we obtain with the Einstein coefficients $A_{\text{rot}} = 6.1 \cdot 10^{-6}$ and $3.4 \cdot 10^{-5} \text{ s}^{-1}$ for the $J = 4-3$ and $7-6$ rotational transitions, $A_{v=1 \rightarrow 0} \sim 20 \text{ s}^{-1}$ (Kirby-Docken & Liu 1978), and the condition $T_{\text{dust}} \gtrsim 3070 \text{ K} / \ln [A_{v=1 \rightarrow 0} / A_{\text{rot}}]$ (see Eq. 6 of Carroll & Goldsmith 1981; $\nu_{v=1 \rightarrow 0} \sim 6.4 \cdot 10^{13} \text{ Hz}$) a minimum dust temperature of $T_{\text{dust}} \sim 200 \text{ K}$. This is much larger than $T_{\text{dust}} = 48 \text{ K}$, estimated by Hughes et al. (1994) and Colbert et al. (1999). The condition for efficient pumping by infrared photons is therefore, if at all, only fulfilled for a small part of the molecular complex in the central region of M 82 (cf. McLeod et al. 1993). Adopting in spite of this $T_{\text{dust}} \sim 200 \text{ K}$, the radiative pumping rate becomes $B_{v=0 \rightarrow 1} u_{v=1-0} \sim 10^{-15} \text{ s}^{-1}$ (or less, if beam dilution plays a role). This is negligible in comparison with the collisional pumping rate.

References

- Aalto S., Radford S.J.E., Scoville N.Z., Sargent A.I., 1999, In: Barnes J.A., Sanders D.B. (eds.) IAU Symp. 186, Galaxy Interactions at Low and High Redshift. Kluwer Academic Publishers, Dordrecht, p. 231
- Achtermann J.M., Lacey J.H., 1995, ApJ 439, 163
- Alton P.B., Davies J.I., Bianchi S., 1999, A&A 343, 51
- Baan W.A., Henkel C., Schilke P., Mauersberger R., Güsten R., 1990, ApJ 353, 132
- Baars J.W.M., Martin R.N., 1996, Rev. Mod. Astron. 9, 111
- Barvainis R., Maloney P., Antonucci R., Alloin D., 1997, ApJ 484, 695
- Blake G.A., Sutton E.C., Masson C.R., Phillips T.G., 1987, ApJ 315, 621
- Brouillet N., Schilke P., 1993, A&A 277, 381
- Carlstrom J.E., 1988, In: Pudritz R.E., Fich M. (eds.) Galactic and Extragalactic Star Formation. Kluwer Academic Publishers, Dordrecht, p. 571
- Carroll T.J., Goldsmith P.F., 1981, ApJ 245, 891
- Casoli F., Dupraz C., Combes F., 1992, A&A 264, 55
- Castets A., Duvert G., Dutrey A., et al., 1990, A&A 234, 469
- Castor J.I., 1970, MNRAS 149, 111
- Chin Y.-N., Henkel C., Langer N., Mauersberger R., 1999, ApJ 512, L143
- Colbert J.W., Malkan M.A., Clegg P.E., et al., 1999, ApJ 511, 721
- Dahmen G., Hüttemeister S., Wilson T.L., Mauersberger R., 1998, A&A 331, 959
- De Jong T., Shih-I Chu, Dalgarno A., 1975, ApJ 199, 69
- Dietz R.D., Smith J., Hackwell J.A., Gehr R.D., Grasdalen G.L., 1986, AJ 91, 758
- Dietz R.D., Gehr R.D., Jones T.J., et al., 1989, AJ 98, 1260
- Downes D., 1989, In: Appenzeller I., Habing H., Léna P. (eds.) Evolution of Galaxies – Astronomical Observations. Lecture Notes in Physics 333, Springer Verlag, Berlin, p. 353
- Downes D., 1999, Rev. Mod. Astron. 12, 69
- Farquhar P.R.A., Millar T.J., Herbst E., 1994, MNRAS 269, 641
- Fux R., 1997, A&A 327, 983
- Fux R., 1999, A&A 345, 787
- Gerin M., Phillips T.G., 1998, ApJ 509, L17
- Gierens K.M., Stutzki J., Winnewisser G., 1992, A&A 259, 271
- Green S., Chapman S., 1978, ApJS 37, 169
- Grevesse N., Sauval A.J., Blomme R., 1994, Rabin D.M., Jefferies J.T., Lindsey C. (eds.) IAU Symp. 154, Infrared Solar Physics. Kluwer Academic Publishers, Dordrecht, p. 539
- Groesbeck T.D., Phillips T.G., Blake G.A., 1994, ApJS 94, 147
- Güsten R., 1989, Morris M. (ed.) IAU Symp. 136, The Center of the Galaxy. Kluwer Academic Publishers, Dordrecht, p. 89
- Güsten R., Downes D., 1980, A&A 87, 6
- Güsten R., Serabyn E., Kasemann C., et al., 1993, ApJ 402, 537
- Harris A.I., Hills R.E., Stutzki J., et al., 1991, ApJ 382, L75
- Harrison A., Henkel C., Russell A., 1999, MNRAS 303, 157
- Harrison A., Puxley P., Russell A., Brand P., 1995, MNRAS 277, 413
- Helfer T.T., Blitz L., 1997, ApJ 478, 233
- Henkel C., Güsten R., Gardner F.F., 1985, A&A 143, 148
- Henkel C., Baan W.A., Mauersberger R., 1991, A&AR 3, 47
- Henkel C., Mauersberger R., 1993, A&A 274, 730
- Henkel C., Whiteoak J.B., Mauersberger R., 1994, A&A 284, 17
- Henkel C., Chin Y.-N., Mauersberger R., Whiteoak J.B., 1998, A&A 329, 443
- Hollenbach D.J., Tielen A.G.G.M., 1997, ARA&A 35, 179
- Howe J.E., Jaffe D.T., Grossman E.N., et al., 1993, ApJ 410, 179
- Hughes D.H., Gear W.K., Robson E.I., 1994, MNRAS 270, 641
- Hüttemeister S., Dahmen G., Mauersberger R., et al., 1998, A&A 334, 646
- Israel F.P., Baas F., 1999, A&A 351, 10
- Israel F.P., White G.J., Baas F., 1995, A&A 302, 343
- Kawamura J., Blundell R., Tong C.-Y.E., et al., 1999, IEEE Trans. on Appl. Superconductivity 9, 3753
- Kikumoto T., Taniguchi Y., Nakai N., et al., 1998, PASJ 50, 309
- Kirby-Docken K., Liu B., 1978, ApJS 36, 359
- Knapp G.R., Phillips T.G., Huggins P.J., Leighton R.B., Wannier P.G., 1980, ApJ 240, 60
- Köster B., Störzer H., Stutzki J., Sternberg A., 1994, A&A 284, 545
- Kronberg P.P., Biermann P., Schwab F.R., 1985, ApJ 291, 693
- Krügel E., Chini R., Klein U., et al., 1990, A&A 240, 232
- Larkin J.E., Graham J.R., Matthews K., et al., 1994, ApJ 420, 159
- Larson R.B., 1981, MNRAS 194, 809
- Lester D.F., Carr J.S., Joy M., Gaffney N., 1990, ApJ 352, 544
- Lo K.-Y., Cheung K.W., Masson C.R., et al., 1987, ApJ 312, 574
- Loiseau N., Nakai N., Sofue Y., et al., 1990, A&A 228, 331
- Loiseau N., Reuter H.-P., Wielebinski R., Klein U., 1988, A&A 200, L1
- Lord S.D., Hollenbach D.J., Haas M.R., et al., 1996, ApJ 465, 703
- Lugten J.B., Watson D.M., Crawford M.K., Genzel R., 1986, ApJ 311, L51
- Mauersberger R., Henkel C., 1989, A&A 223, 79
- Mauersberger R., Henkel C., 1993, Rev. Mod. Astr. 6, 69
- Mauersberger R., Guélin M., Martín-Pintado J., et al., 1989, A&AS 79, 217
- Mauersberger R., Henkel C., Whiteoak J.B., Chin Y.-N., Tieftrunk A.R., 1996a, A&A 309, 705
- Mauersberger R., Henkel C., Wielebinski R., Wiklind T., Reuter H.-P., 1996b, A&A 305, 421
- Mauersberger R., Henkel C., Walsh W., Schulz A., 1999, A&A 341, 256

- McLeod K.K., Rieke G.H., Rieke M.J., Kelly D.M., 1993, *ApJ* 412, 111
- Morris M., Serabyn E., 1996, *ARA&A* 34, 645
- Nakai N., Hayashi M., Handa T., Sofue Y., Hasegawa T., 1986, *PASJ* 38, 603
- Nakai N., Hayashi M., Handa T., Sofue Y., Hasegawa T., 1987, *PASJ* 39, 685
- Neininger N., Guélin M., Klein U., Garcia-Burillo S., Wielebinski R., 1998, *A&A* 339, 737
- Nieten Ch., Dumke M., Beck R., Wielebinski R., 1999, *A&A* 347, L5
- O'Connell R.W., Gallagher J.S., Hunter D.A., Colley W.N., 1995, *ApJ* 446, L1
- Oka T., Hasegawa T., Hayashi M., Handa T., Sakamoto S., 1998a, *ApJ* 493, 730
- Oka T., Hasegawa T., Sato F., Tsuboi M., Miyazaki A., 1998b, *ApJS* 118, 455
- Olofsson H., Rydbeck G., 1984, *A&A* 136, 17
- Omont A., Petitjean P., Guilloateau S., et al., 1996, *Nat* 382, 428
- Ossenkopf V., 1997, *New Astr.* 2, 365
- Paglione T.A.D., Jackson J.M., Ishizuki S., 1997, *ApJ* 484, 656
- Petitpas G.R., Wilson C.D., 1998, *ApJ* 503, 219
- Phillips J.P., Mampaso A., 1989, *A&A* 218, 24
- Sage L.J., Isbell D.W., 1991, *A&A* 247, 320
- Sakai S., Madore B.F., 1999, *ApJ* 526, 599
- Schilke P., Carlstrom J.E., Keene J., Phillips T.G., 1993, *ApJ* 417, L67
- Schulz A., Henkel C., Beckmann U., et al., 1995, *A&A* 295, 183
- Scoville N.Z., Solomon P.M., 1974, *ApJ* 187, L67
- Seaquist E.R., Carlstrom J.E., Bryant P.M., Bell M.B., 1996, *ApJ* 465, 691
- Seaquist E.R., Frayer D.T., Bell M.B., 1998, *ApJ* 507, 745
- Shen J., Lo K.-Y., 1995, *ApJ* 445, L99
- Smith P.A., Brand P.W.J.L., Mountain C.M., Puxley P.J., Nakai N., 1991, *MNRAS* 252, 6
- Sofue Y., Reuter H.-P., Krause M., Wielebinski R., Nakai N., 1992, *ApJ* 395, 126
- Solomon P.M., Downes D., Radford S.J.E., 1992a, *ApJ* 387, L55
- Solomon P.M., Downes D., Radford S.J.E., 1992b, *ApJ* 398, L29
- Stacey G.J., Geis N., Genzel R., et al., 1991, *ApJ* 373, 423
- Stahl O., Wilson T.L., 1992, *A&A* 254, 327
- Stahl O., Wilson T.L., Henkel C., Appenzeller I., 1989, *A&A* 221, 321
- Störzer H., Stutzki J., Sternberg A., 1996, *A&A* 310, 592
- Störzer H., Zielinsky M., Stutzki J., Sternberg A., 2000, *A&A*, submitted
- Stutzki J., Graf U.U., Haas S., et al., 1997, *ApJ* 477, L33
- Suchkov A., Allen R.J., Heckman T.M., 1993, *ApJ* 413, 542
- Sutton E.C., Masson C.R., Phillips T.G., 1983, *ApJ* 275, L49
- Taniguchi Y., Ohyama Y., 1998, *ApJ* 507, L121
- Telesco C.M., Campins H., Joy M., Dietz K., Decher R., 1991, *ApJ* 369, 135
- Telesco C.M., Gezari D.Y., 1992, *ApJ* 395, 461
- Tilanus R.P.J., Tacconi L.J., Sutton E.C., et al., 1991, *ApJ* 376, 500
- Turner J.L., Martin R.N., Ho P.T.P., 1991, *ApJ* 367, 677
- van Dishoeck E.F., Blake G.A., 1998, *ARA&A* 36, 317
- Völk H.J., Klein U., Wielebinski R., 1989, *A&A* 213, L12
- Watson W.D., Anichich V.G., Huntress W.T., 1976, *ApJ* 205, L165
- Weliachew L., Fomalont E.B., Greisen E.W., 1984, *A&A* 137, 335
- White G.J., Ellison B., Claude S., Dent W.R.F., Matheson D.N., 1994, *A&A* 284, L23
- White R.E., 1977, *ApJ* 211, 744
- Wild W., Harris A.I., Eckart A., et al., 1992, *A&A* 265, 447
- Wilson C.D., Howe J.E., Balogh M.L., 1999, *ApJ* 517, 174
- Wilson T.L., Rood R.T., 1994, *ARA&A* 32, 191
- Wolfire M.G., Tielens A.G.G.M., Hollenbach D., 1990, *ApJ* 358, 116
- Young J.S., Scoville N.Z., 1984, *ApJ* 287, 153